Copyright

by

Christian G. Parthey

2007

# Pulsed Magnetic Slowing of Supersonic Beams

by

**Christian G. Parthey,**

**Thesis**

Presented to the Faculty of the Graduate School of

The University of Texas at Austin

in Partial Fulfillment

of the Requirements

for the Degree of

**Master of Arts**

**The University of Texas at Austin**

December 2007

# Pulsed Magnetic Slowing of Supersonic Beams

**Approved by**
**Supervising Committee:**

_____

_____

# Acknowledgments

First, I want to thank my supervisor Prof. Mark Raizen. Mark, I really enjoyed working in your group. You gave me the opportunity to contribute to something great and made me feel comfortable with your way of keeping a good balance between freedom and advice. Thank you for your support here in Austin and beyond.

Dr. Edvardas Narevicius, Adam Libson and Isaac Chavez are my co-workers on the slowing project and everything we achieved was a group effort.

Ed, you've been the post doc in the group. You made us focus on the important things and asked those questions which are awkward in the beginning, but ultimately lead to a deeper understanding. I want to thank you for guiding my thoughts, and for your advice as to my future studies. We also became friends and I had a great time with you and your family. I want to take the opportunity to thank you, Julia and Yoav for the wonderful surprise with a birthday cake and I hope your family will always have so much joy that you can share it with others.

Adam, I really enjoyed working with you since I had the impression that we were complementing each other very well. Your ability to explain in a clear way was very helpful, particularly when we were developing new ideas. Beyond the lab we became good friends, you helped me to understand many parts of the American culture, and I am very glad that you introduced me to rock climbing. I wish you the very best for your future both for your graduate studies and in private life.

Isaac, you joined the group long time before I came to Austin and it was fun

to watch you growing from the "small undergrad" to a full group member who just gets things done. Thanks for watching my back, buddy, especially while working with the high voltage boxes.

Max Riedel is a Würzburg student from the former generation and our time in Austin overlapped. Max, you were the familiar part when I first arrived in Austin as we had already met in Würzburg. Since we had a similar background you were able to help me a lot by explaining the course of work, translating special vocabulary, and introducing me to people. I hope that our ways are going to cross again in Germany.

Prof. Uzi Even is our collaborator at Tel Aviv University and was visiting our lab during my first two months. Uzi, I am very glad that I had the opportunity to meet you in Austin. You made it very easy for me to join the rotor experiment since you always answered my questions and gave me all the numerous tips that make an experimentalist's daily life much easier. Thank you for widening my horizon both concerning life and work.

I want to thank the whole Raizen group, Hrishikesh Kelkar, Tongcang Li, David Medellin, Gabriel Price, Travis Bannerman, Kirsten Viering, Charlotte Sanders, Christoph Schaeff and Bree Guerra, for the great atmosphere. You all contributed to make my stay more enjoyable and productive.

I want to thank my girlfriend Uli for all the numberless small things that help me every day and the support I found in her.

I thank my parents who always supported my interest in physics and made it possible for me to study.

I thank my former roommate Hendrik Bentmann for interesting discussions on a lot of physical problems, asking me critical questions about our experiment and sharing our successes.

I am grateful to Olga Vera and Elena Simmons who took care of the paper-

work during my stay and who do a great job in making sure we have enough time to do research. I also want to thank our Graduate Coordinator Carol Noriega for reminding me of all the deadlines one has to meet during one and a half years of graduate studies.

The machine shop did a terrific job on building the parts for our two slower generations in a very short period of time and the cryoshop and supply room helped to keep our lab running. Thanks for all the help, guys!

I would like to thank Prof. Manfred Fink here in Austin as well as Prof. Fakher Assaad, Prof. Manfred Böhm and Prof. Hansheinrich Langhoff in Würzburg for organizing the exchange program between the two universities. I greatly enjoyed my stay at the University of Texas at Austin and hope that many more students will get this opportunity.

I acknowledge funding from the DAAD during my stay in Austin and want to thank the College of Natural Science for supporting me through the C. Paul Boner Graduate Fellowship in Physics.

Christian G. Parthey

*The University of Texas at Austin*
*December 2007*

# Pulsed Magnetic Slowing of Supersonic Beams

Christian G. Parthey, M.A.
The University of Texas at Austin, 2007

Supervisor: Mark G. Raizen

Supersonic beams provide a source of cold atoms where laser cooling is not applicable. Although the atoms' temperature in the co-moving frame is in the sub-kelvin range their velocity is on the order of several hundreds of meters per second. This thesis describes the experimental realization of a novel method to slow atoms and molecules with permanent magnetic moments using pulsed magnetic fields. The method is suitable for most elements since most atomic species are paramagnetic, and can also be applied to certain molecules, as well as electronically excited metastable states and most radicals. We show the slowing of metastable neon in a proof of principle experiment where the mean velocity is reduced from $461.0 \pm 7.7\,\mathrm{m/s}$ to $403 \pm 16\,\mathrm{m/s}$ in 18 stages. A second setup with 64 stages is now operating and allows us to stop metastable neon in principle. Preliminary results showing slowing from $447 \pm 3\,\mathrm{m/s}$ to $136 \pm 5\,\mathrm{m/s}$ with an efficiency of up to $3.9\,\%$ are included here, and the slower has been shown to generate atoms as slow as $50\,\mathrm{m/s}$.

We find that the slowing efficiency depends strongly on the switching phase.

In addition to the experimental results described above, we present simulations of a moving trap which allows trapping and decelerating at the same time.

# Contents

**Acknowledgments** iv

**Abstract** vii

**Table of Contents** x

**Chapter 1 Introduction** 1

**Chapter 2 Principle of Operation** 3

2.1 Supersonic Beams . . . 3

2.1.1 The Pulsed Supersonic Nozzle . . . 7

2.1.2 Gas Discharge . . . 8

2.2 Pulsed Magnetic Slowing . . . 9

2.2.1 Atoms in External Magnetic Fields . . . 10

2.2.2 Coil Inductance, Eddy Currents, and Hysteresis . . . 11

2.2.3 Field Characterization . . . 13

2.2.4 Phase Stability . . . 13

2.3 Beam Detection . . . 16

**Chapter 3 Monte Carlo Beam Simulations** 17

3.1 Pulsed Magnetic Slowing . . . 17

3.2 Moving Trap . . . 19

**Chapter 4 18 Stage Magnetic Slower** 22

4.1 Setup . . . 22

4.1.1 Coil Assembly . . . 22

4.1.2 Driver Electronics . . . 26
4.1.3 Magnetic Field Characteristics . . . 29
4.1.4 Pulse Generation . . . 29
4.2 Results . . . 30

**Chapter 5 64 Stage Magnetic Slower** **33**
5.1 Setup . . . 33
5.1.1 Coil Assembly . . . 33
5.1.2 Vacuum Chamber and Coil Mount . . . 36
5.1.3 Driver Electronics . . . 40
5.1.4 Magnetic Field Characteristics . . . 41
5.1.5 Pulse Generation . . . 44
5.2 Results . . . 44

**Chapter 6 Conclusions** **49**

**Bibliography** **50**

**Vita** **53**

# Chapter 1

# Introduction

It has long been recognized that controlling the velocity of cold atoms and molecules in supersonic beams would provide a means for trapping of species where no other methods are currently available. Many atoms and molecules can be entrained or seeded into supersonic beams and are cooled to sub-kelvin temperatures. However, internal energy lost in adiabatic expansion is converted to kinetic energy leading to high velocities in the laboratory frame. Velocities of supersonic beams vary between a few hundred to several thousand meters per second, depending mainly on the source temperature and carrier gas' atomic or molecular weight [1]. The temperatures reached in supersonic expansion can be as low as several tens of millikelvin. There have been two general approaches to slowing of supersonic beams. One school of thought treats the atoms and molecules in the beam as billiards, using motion of other objects or particles to slow the cold atoms. Several notable examples of this method include the slowing of helium via specular reflection from a receding crystal [2], mounting the supersonic source on a spinning rotor [3], and elastic collisions of crossed beams [4]. The other approach uses interactions with time varying external fields. This includes the Stark decelerator [5] and slowing with pulsed laser fields [6].

In this work we present the experimental realization of a new slowing scheme using pulsed magnetic fields to decelerate paramagnetic species. This method relies on the Zeeman shift and thus, is applicable to most ground state atoms, most radicals and some molecules like $O_2$. Although noble gases are diamagnetic in their ground state, they can be excited into a metastable state which has a magnetic moment.

We describe the design of our slowing apparatus in detail and present data which show the deceleration of metastable neon from $447 \pm 3$ m/s to $136 \pm 5$ m/s with an efficiency of up to 3.9 %. We find that the slowing efficiency depends strongly on the switching phase.

In parallel to our work, slowing of atomic hydrogen and deuterium with seven stages has been demonstrated [7, 8].

This thesis is arranged as follows:

In the second chapter we present a short summery about supersonic beams and key features of our cryogenic pulsed supersonic nozzle. We explain how we create paramagnetic metastable neon which can be slowed with our slower. We start the section about pulsed magnetic slowing by outlining the operating principles. We then give an overview of important theoretical aspects used in the pulsed magnetic slower, including the Zeeman shift in low and high magnetic fields, effects occurring in switched magnetic fields and how the Faraday effect can be used to characterize magnetic fields with MHz time resolution. We complete the section about pulsed magnetic slowing by explaining its operation on the basis of phase stability.

In chapter 3 we present Monte Carlo beam simulations of pulsed magnetic slowing that were performed on the example of molecular oxygen. The feasibility of a fast moving magnetic trap which can trap atoms and molecules at 250 m/s and which can then be slowed down to decelerate the trapped species is demonstrated based on simulations.

In chapter 4 we present design and results for two different pulsed magnetic slowing apparatus. We first describe our 18 stage slower which was placed in an existing vacuum chamber. Along with the coil design we explain our driving circuit and characterize our magnetic fields. We decelerate metastable neon from $461.0 \pm 7.7$ m/s to $403 \pm 16$ m/s in 18 stages.

In chapter 5 we describe the coil setup, the vacuum system and the driver circuitry of a 64 stage slower. The magnetic fields are characterized using the Faraday effect. We present results showing the slowing from $447 \pm 3$ m/s to $132 \pm 5$ m/s and observe that the slow atom numbers strongly depend on the switching phase which we adjust during the slowing process to obtain higher atom numbers.

# Chapter 2

# Principle of Operation

In this chapter we explain the mechanism on which our slowing apparatus is based, outline briefly the underlying physics, and give detailed descriptions of the individual parts of the setup. We start with the theory of supersonic beams, discuss our supersonic nozzle, and talk about the DC discharge that excites the neon into its metastable state. We then describe the principle of pulsed magnetic slowing, the effects atoms experience in external magnetic fields, and parasitic effects in electromagnetic coils. We outline a method to characterize high magnetic fields with MHz resolution and approach the operation of the pulsed magnetic slower from the standpoint of phase stability. Finally, we present our detection scheme.

## 2.1 Supersonic Beams

Generally, atomic beams are generated by letting a gas escape from a big reservoir tank at pressure $p_r$ through a small aperture into a vacuum chamber ($p_v$). If the mean free path is larger than the aperture the resulting beam is effusive, i.e. it has a Maxwellian velocity distribution $f(v)$

$$f(v) = 4\pi \left(\frac{m}{2\pi kT}\right)^{3/2} v^2 \exp\left(\frac{-mv^2}{2kT}\right) \tag{2.1}$$

where $m$ is the mass of a single gas particle, $k$ is the Boltzmann constant and $T$ the system's temperature. The velocity spread $\sigma_v$ is given by

$$\sigma_v = \sqrt{kT/m} \tag{2.2}$$

and is quite broad. For neon at 77 K one calculates the most probable velocity $v_0 = 253\,\mathrm{m/s}$ and a velocity spread $\sigma_v = 179\,\mathrm{m/s}$.

However, raising the pressure to a point where the mean free path becomes significantly smaller than the nozzle diameter one enters the regime of supersonic expansions.

This technique is widely used to create high intensity beams of atoms, molecules and clusters. In the proper gas regimes, supersonic expansions reduce the velocity spread in the co-moving frame, i.e. the temperature, and lower the rotational and vibrational temperature where applicable. In our experiment supersonic expansion is the only cooling mechanism and phase space densities achieved by the supersonic beam place an upper limit since our slowing method conserves phase space density.

Supersonic expansion is similar to the adiabatic expansion in a heat engine where a gas does work on a piston, however in this case the gas does work on itself. The pressure differential accelerates the gas during the expansion, leading to a beam of atoms with a high mean velocity and a low velocity spread. At low differential pressures, an increase in the reservoir pressure leads to a higher beam velocity. However, if one reaches a critical pressure difference the atoms are accelerated to the local speed of sound and can no longer respond to local boundary conditions. Therefore, the pressure at the nozzle exit is no longer given by the pressure in the vacuum chamber $p_v$ but is a fraction of the reservoir pressure $p_r$. Thus, further increase of $p_r$ does not result in any increase in the beam velocity. This final beam velocity $v_\infty$ can be approximated by conservation of energy [9]:

$$NkT_0 + W = \frac{1}{2}Mv^2 + NkT \tag{2.3}$$

where $N$ is the number of atoms, $k$ is the Boltzmann constant, $T_0$ is the reservoir temperature, $W$ is the work that was put into the gas compressing it into the reservoir, $M$ is the total mass of the expanding atoms, $v$ is the velocity of the atomic beam, and $T$ is the expanded atoms' temperature. Dividing equation (2.3) by $M$

and using the ideal gas equation as well as the definition of enthalpy $h = u + pV$ we find

$$h_0 = \frac{v^2}{2} + h \tag{2.4}$$

where $h_0$ and $h$ are the enthalpy per unit mass of the gas in the reservoir and after expansion, respectively. Using

$$\frac{dh}{dT} = C_p \tag{2.5}$$

where we assume the specific heat $C_p$ to be constant in temperature the final beam velocity yields

$$v_\infty = \sqrt{2C_p(T_0 - T)}. \tag{2.6}$$

For an ideal gas the specific heat can be expressed in terms of the ratio $\gamma = C_p/C_V$ of the specific heats of constant pressure and volume:

$$C_p = \frac{\gamma}{\gamma - 1}\,\frac{R}{m} \tag{2.7}$$

where $R$ is the ideal gas constant, $m$ is the mass of the expanding atom and $\gamma = 5/3$ for an ideal gas. Hence, the final beam velocity from a supersonic expansion can be written as

$$v_\infty = \sqrt{2\frac{\gamma}{\gamma - 1}\,\frac{R}{m}(T_0 - T)}. \tag{2.8}$$

With

$$\frac{T}{T_0} = \left(\frac{p}{p_0}\right)^{\frac{\gamma-1}{\gamma}} \tag{2.9}$$

we can re-write equation (2.8) in terms of the pressures in the reservoir $p_r$ and the vacuum chamber $p_v$:

$$v_\infty = \sqrt{2\frac{\gamma}{\gamma - 1}\,\frac{R\,T_0}{m}\left(1 - \left(\frac{p_v}{p_r}\right)^{\frac{\gamma-1}{\gamma}}\right)}. \tag{2.10}$$

One can see that typical beam velocities are on the order of several hundreds to a few thousands of meters per second, depending on the reservoir temperature and the expanding species' mass. Since we want to use the supersonic beam for a slowing experiment it is advantageous to start out with a beam of low velocity. On the one hand this can be achieved by reducing the reservoir's temperature. This approach

| Species | Valve Temperature | Mean Velocity | Velocity Spread ($\sigma_v$) |
|---|---|---|---|
| He | 300 K | 1800 m/s | 22 m/s |
| He | 77 K | 900 m/s | 11 m/s |
| Ne | 300 K | 800 m/s | 11 m/s |
| Ne | 77 K | 400 m/s | 12 m/s |
| Ar | 300 K | 600 m/s | 17 m/s |
| Kr | 300 K | 450 m/s | 11 m/s |
| Xe | 350 K | 390 m/s | 9.8 m/s |

Table 2.1: Experimental beam characteristics for our supersonic valve [10].

can be easily achieved using a cryogenic valve and one is only limited by the used gas condensation temperature. One the other hand one can use a heavier gas which in general is not easy to realize as the choice of gas is usually determined by the experiment. However, it is possible to dilute the desired atoms or molecules with a heavier "carrier gas". In this case, $m$ in equation (2.8) must be replaced by the average mass of the carrier gas and the gas of interest $\bar{m} = \sum_i x_i m_i$, where $x_i$ are the fractions of the gases and $m_i$ their masses. Typical fractions of the carrier gas vary from 50 % to 99 % allowing a compromise between flux and beam velocity. Nevertheless, one has to be careful with the choice of the carrier gas. If the mass ratio between the lighter and heavier gas becomes to small the lighter species is pushed out of the beam during supersonic expansion, i.e. the lighter atom travels on the outer boundary of the beam resulting in a very broad velocity distribution.

Besides diluting the desired gas with a carrier gas which is known as seeding, it is also possible to introduce a gas into the supersonic beam by crossing it with another supersonic or effusive beam right after the nozzle exit. This process is called entrainment and although it is experimentally harder to realize than seeding, it is more general as instead of a beam one can place a solid close to the nozzle exit and use laser ablation to evaporate the solid.

As anyone working with atomic or molecular beams can confirm, making good atomic or molecular beams is an art and back of the envelope predictions are hard to make. Therefore we give some experimental examples for mean velocity and spread in table 2.1. The equations given above are only strictly valid for continuous nozzles although nowadays most supersonic valves are pulsed to achieve higher brightnesses.

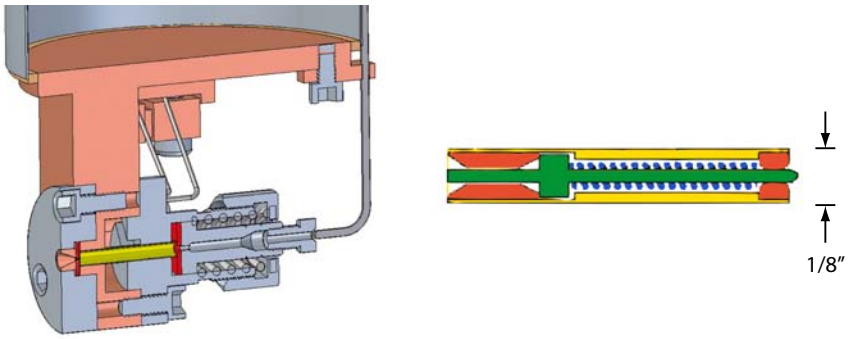


Figure 2.1: Schematic view of the supersonic nozzle we use. *Left:* A stainless steel cryostat allows cooling the trumpet shaped nozzle to liquid nitrogen temperature. The valve mechanism is enclosed in a high pressure steel tube (*yellow*) which is sealed by two kapton washers (*red*). A strong spring from the back guarantees a good seal up to pressures of 100 atm. A coil (not depicted) generates a magnetic field of up to 2.5 T to open the valve. *Right:* Presented is a detailed view of the high pressure tube. The valve blocking plunger (*green*) is guided by two ceramic pieces (*orange*). The electromagnetic coil pulls the plunger back by about 150 $\mu$m. It is returned into its sealing position by a small spring (*blue*) after the coil is switched off. Taken from [13]

### 2.1.1 The Pulsed Supersonic Nozzle

Starting point of the experiment is a supersonic beam generated by our cryogenic high intensity supersonic nozzle [11, 12]. Recent developments by Prof. Uzi Even from Tel Aviv University have lead to remarkable key features of our supersonic nozzle. It allows opening times as short as 10 $\mu$s full width at half maximum (FWHM), a repetition rate of up to 40 Hz and the possibility of cryogenic (20 K) operation. Using backing pressures of up to 100 atm generates beams in helium which are very directional (half angle of 7°) and monochromatic (velocity spreads of smaller than 1 %).

A schematic of the valve is presented in figure 2.1. The trumpet shaped nozzle with an opening of 200 $\mu$m is mounted in a copper block cooled by the attached cryostat. A high pressure steel tube (*yellow*) which is sealed at its ends by kapton washers (*red*) contains the valve mechanism (compare figure 2.1 *right*): The blocking plunger (*green*) is guided by two ceramic pieces (*orange*) and pushed

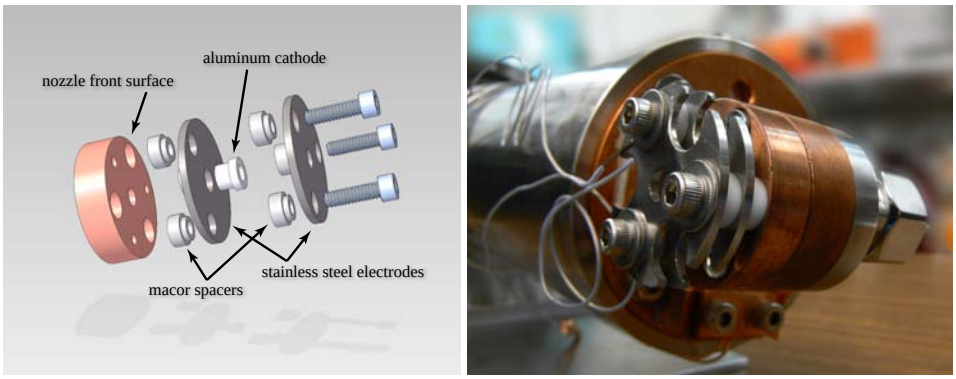


Figure 2.2: Schematic of the discharge mounted on the front face of the nozzle (*left*) and photograph of the assembly (*right*).

to the front by a small spring (*blue*). An electromagnetic coil (not shown) pulls the plunger about 150 $\mu$m back and it returns within 15 $\mu$s to its sealing position.

The atom flux $\Phi$ released from the nozzle can be estimated by

$$\Phi = \frac{\rho v}{4} \tag{2.11}$$

where $\rho$ is the number density and $v$ the beam's mean velocity. At 77 K and a backing pressure of 30 atm the resulting beam of helium has a mean velocity of approximately 900 m/s resulting in a flux of $\Phi \approx 6 \times 10^{29}$ atoms/(m$^2$s). Using the nozzle diameter of 200 $\mu$m and an opening time of 10 $\mu$s the brightness of the beam can be estimated to $2 \times 10^{17}$ atoms/shot which leads us at a repetition rate of 40 Hz to $8 \times 10^{18}$ atoms/s.

### 2.1.2 Gas Discharge

We use a pulsed DC discharge between a stainless steel plate and a hollow aluminum electrode (see figure 2.2) to excite neon into its metastable $^3P_2$ state. While the front stainless steel plate and the nozzle itself are kept grounded we can apply a voltage of up to 2 kV on the aluminum electrode which is mounted into another stainless steel plate. The aluminum electrode is equally spaced to nozzle and front steel plate by 1 mm and has a bore of 4 mm. The discharge occurs between the front steel plate and the aluminum cathode as can be observed by eye through a view port.

In order to initiate and stabilize the discharge a tungsten filament is mounted

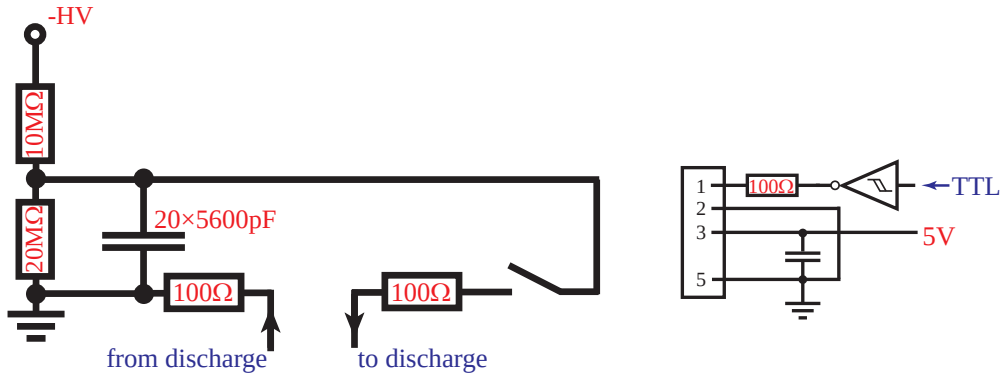


Figure 2.3: Schematic of the discharge driving circuit. The digital part driving the switch is depicted on the right side.

2 cm off the beam line and 2 cm in front of the first steel plate. It serves as electron emitter. The filament is biased at −100 V and driven with a current of 3.5 A. The circuit driving the discharge is shown in figure 2.3. The 0.112 $\mu$F capacitor bank is charged through a 10 MΩ resistor, limiting the charging current to 0.2 mA. Since a typical discharge pulse is on the order of 3 $\mu$s a repetition rate of up to 5 Hz is possible.

The digital signal opening the high voltage switch [14] is inverted since the switch is open if it gets a +5 V signal.

## 2.2 Pulsed Magnetic Slowing

The operational principle of our magnetic decelerator is based on the Zeeman effect, similar to the way the pulsed electric field decelerator is based on the DC Stark effect. The electronic states of atoms or molecules that have a non-zero total angular momentum split into magnetic sublevels in the presence of magnetic fields. As our slowing is optimized for low field seeking electronic states, we will now describe such an atom's interaction with our coils.

As a low field seeking atom moves along the axis of an energized electromagnetic coil it loses kinetic energy by climbing the magnetic "hill". If the coil were left on as the atom passed through, it would ride the magnetic "hill" down and gain back the same amount of energy lost. However, if we switch off the current flowing through the coil suddenly as the atom passes through the center, the atom loses

the amount of kinetic energy equal to the Zeeman shift at the top of the "hill". The process can be repeated again with another coil until the particle comes to rest in the laboratory frame. The slowing process conserves phase space density and only reduces a specific target velocity of the distribution without affecting the temperature. The stopped atoms can then be transferred into a magnetic trap.

### 2.2.1 Atoms in External Magnetic Fields

Atoms interact with external magnetic fields due to their magnetic moment. The (weak field) Zeeman splitting in an external magnetic field $B$ according to first order perturbation theory is given by

$$\Delta E = -m_j g_j \mu_B B \tag{2.12}$$

where $m_j$ is the projection of the total angular momentum onto the magnetic field axis, $\mu_B$ the Bohr magneton and $g_j$ the Landè factor. The latter is given by

$$g_j = 1 + \frac{J(J+1) + S(S+1) - L(L+1)}{2J(J+1)} \tag{2.13}$$

with principal quantum numbers $S$, $L$, $J = S + L$.

If the Zeeman splitting (2.12) becomes comparable to the fine structure correction spin and angular momentum decouple and one reaches the Paschen-Back (strong field Zeeman) regime; the quantum number $J$ is not a good quantum number any more and in that case the splitting is given by

$$\Delta E = (m_l + 2\, m_s)\mu_B B. \tag{2.14}$$

Due to different possible orientations of the projection of total angular and spin momenta with respect to external magnetic fields, atoms can minimize their energy in high field regions (so called high field seekers) or in low field regions (so called low field seekers). Our slowing scheme works for low field seekers only.

Although the ground state of neon, $1s^2 2s^2 2p^6$, is diamagnetic due to its closed shell structure and does not experience a Zeeman splitting, it can be excited to the metastable $1s^2 2s^2 2p^5 3s^1$ electronic configuration. The life time of this state is 14.7 s [15], which is sufficient for our experiments since typical times of flight are on the

order of several milliseconds. We slow the $^3P_2$ state, where $m_J = 1, 2$ are low field seeking states and can be slowed with our apparatus. As a higher $m_J$ results in a higher Zeeman splitting we time our slower to select the $m_J = 2$ state. Due to five possible values for $m_J$ we lose 80 % of the atoms in the original peak just because they are in the wrong atomic state. The Landé factor for the $^3P_2$ state is 1.5 which leads to an effective magnetic moment of $\mu = 3\,\mu_B$ where $\mu_B$ is the Bohr magneton. This holds for low magnetic fields were the Zeeman level splitting is small compared to the fine structure of the $2p^5 3s^1$ configuration. Note that the neon $^3P_2$ metastable state's the energy shift $\Delta E$ is the same in both the Zeeman and the Paschen-Back regime, namely $\Delta E = -3\mu_B B$. For the magnetic field in our two slower models $B_1 = 3.6\ T$ and $B_2 = 5.2\ T$ the splittings become

$$\Delta E_1 = -0.625\,\text{meV}\ (-5.04\,\text{cm}^{-1}) \tag{2.15}$$

$$\Delta E_2 = -0.903\,\text{meV}\ (-7.28\,\text{cm}^{-1}). \tag{2.16}$$

We do not expect to remove this much energy per slowing stage since target atoms do not experience the peak field when we switch it off.

### 2.2.2 Coil Inductance, Eddy Currents, and Hysteresis

The current in a coil is described by the differential equation for an LR-circuit

$$\frac{d}{dt}I = -\frac{R}{L}I + \frac{R \cdot I_0}{L} \tag{2.17}$$

with the maximum current $I_0$, the resistance $R$, and the inductance $L$ which is given for a solenoid by

$$L = N^2 \cdot \frac{\mu_0 \mu_r l}{2\pi} \cdot \ln\frac{R}{r} \tag{2.18}$$

where $N$ is the number of winding, $\mu_0$ is the vacuum permeability, $\mu_r$ is the relative permeability of the coil core, $l$ is the coil length, $R$ is its outer radius and $r$ is the inner radius. Solving (2.17) for the initial conditions $I(0) = 0$ and $I(0) = I_0$ we obtain the current profiles for switch on and switch off in the coil

$$I(t) = I_0 \cdot \left(1 - e^{-\frac{R}{L}t}\right) \tag{2.19a}$$

$$I(t) = I_0 \cdot e^{-\frac{R}{L}t}. \tag{2.19b}$$

We see that coils switch on and off exponentially and the time constant, $\tau = L/R$, is proportional to the inductance $L$ and the conductivity $\sigma = 1/R$. These switching times neglect the effects of applied voltage differences across the coil, however they illustrate the desirable coil parameters for fast switching. To achieve fast switching times one has to choose a small inductance or a large resistance. Since our experiment requires high currents a high resistance is not desirable. Hence, a small number of windings is preferable (see equation (2.18)). There are two more things we have to keep in mind if we want to build a coil producing a high magnetic field: Ampère's law [16] tells us

$$\vec{\nabla} \times \vec{B} = \mu_0 \vec{j} \tag{2.20}$$

where $\vec{j}$ is the current density. Thus, we want to drive high current within a small area in our coil. From Maxwell's equation

$$\vec{\nabla} \cdot \vec{B} = 0 \tag{2.21}$$

we know that there are no magnetic monopoles, therefore

$$\vec{B}\,(\vec{x}) = \frac{\mu_0}{4\pi} \int I \; d\vec{x}_0 \times \frac{\vec{x} - \vec{x}_0}{|\vec{x} - \vec{x}_0|^3}, \tag{2.22}$$

the magnetic field $\vec{B}$ drops with $r^{-3}$, making small coil bore sizes favorable. These considerations lead to the coil design described in section 4.1.1.

Since we enclose our coil in a permendur [17] shell to confine the magnetic fields well within the coil the field does not follow the current linearly.

Whenever there is a conductive material next to a time dependent B-field an electric field is induced in the material according to the Maxwell equation

$$\vec{\nabla} \times \vec{E} + \frac{\partial \vec{B}}{\partial t} = 0. \tag{2.23}$$

The induced circular currents are known as eddy currents and cause a magnetic field according to equation (2.20) which opposes the change in field following Lenz's law.

Changing magnetic fields in ferromagnetic materials also causes another effect known as hysteresis. Due to the external magnetic field the magnetic dipoles in the material align. When the external field is switched off, the alignment is partially retained, and the material is magnetized.

Permendur was developed to have a high magnetic flux saturation density combined with low hysteresis losses making it a good material for transformers. Its properties depend strongly on the manufacturing process. Since there is not hysteresis data available in the MHz range calculations on switching behavior are not possible. Instead, measurements on the coil itself are performed.

### 2.2.3 Field Characterization

We utilize the Faraday effect to characterize the fields produced in our electromagnetic coils: certain materials, so-called Faraday rotators, rotate the vibrational plane of light if an external magnetic field is applied. The effect is greatest if the B-field is collinear with the light's propagation axis.

The rotation angle in radians is given by the empirical expression

$$\beta = VBd \tag{2.24}$$

where $V$ is the Verdet constant, $B$ the magnetic field and $d$ the distance the light travels through the rotating material [18]. Note that the Verdet constant has a strong wavelength and temperature dependence.

In our experiment we use a terbium gallium garnet crystal (TGG) as the optically active material which has a Verdet constant of $V = -134\,\mathrm{rad\ T^{-1}m^{-1}}$ at a wavelength of 633 nm and room temperature [19]. The minus sign indicates the direction of rotation: Imagine the magnetic field generated by a solenoid wound around the Faraday rotator. If the Verdet constant is negative the plane of vibration is rotated opposite of the current flowing through the coil, regardless of the light propagation direction.

### 2.2.4 Phase Stability

In order to understand the mechanism of pulsed magnetic slowing it is necessary to make oneself familiar with the concept of phase stability. To simplify the problem we will assume an ideal magnetic field that can be switched off instantaneously, and that is switched on long before it switches off.

The idealized potential as seen by a paramagnetic atom travelling through the pulsed magnetic slower as a function of its position $z$ is shown in figure 2.4. The

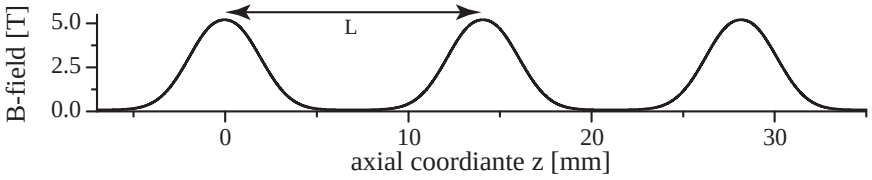


Figure 2.4: Magnetic potential of a paramagnetic atom as a function of $z$ along the beam axis. $L$ is the distance from one center of a coil to the next.

amount of energy the atom loses per stage depends on its position at the time the fields are being switched. We express this position in form of an phase angle $\phi$ which has a periodicity of the length $L$ and is well established in the pulsed electric field decelerator (Stark decelerator) [20] and has its origin in charged particle accelerators [21]. Atoms that experience maximum field right before the field is switched off are assigned a phase angle of $\phi = 90°$ while atoms at the point between two coils when the fields are switched are assigned a phase of $\phi = 0°$. The phases for atoms between these points are assigned as a linear function of this position as the magnetic potential is approximated by a sine function (with offset).

We start with a situation where the fields are switched off with a constant time delay $\Delta t$, i.e. the first coil is switched off after $\Delta t$, the second after $2\Delta t$ and so on. Lets look at an atom at a phase $\phi = 0°$ that travels at a velocity that matches the switching frequency off the magnetic field, meaning $v = L/\Delta t$. This atom can be seen as 'in sync' with the slower. Its phase and velocity are referred to equilibrium phase $\phi_0$ and equilibrium velocity $v_0$, respectively. It can easily be seen that (i) the synchronous atom passes the slower unaffected and (ii) that atoms with slightly different phase and velocity will experience a natural correction towards $\phi_0$ and $v_0$. An atom with a phase slightly larger than $\phi_0$ and a velocity equal to $v_0$ will lose more energy per stage than the synchronous atom. Hence, it will slow down compared to the synchronous atom and therefore its phase will become smaller, until it falls behind. At this point, the situation is reversed and it will lose less energy than the synchronous atom, and so on. This thought experiment shows how atoms with slightly different phase from $\phi_0$ and/or velocity from $v_0$ will oscillate in phase and velocity around the equilibrium values. The atoms are trapped in a one sided potential well travelling at the velocity of the synchronous atom.

In order to decelerate an atom one has to slow down the potential hill, which

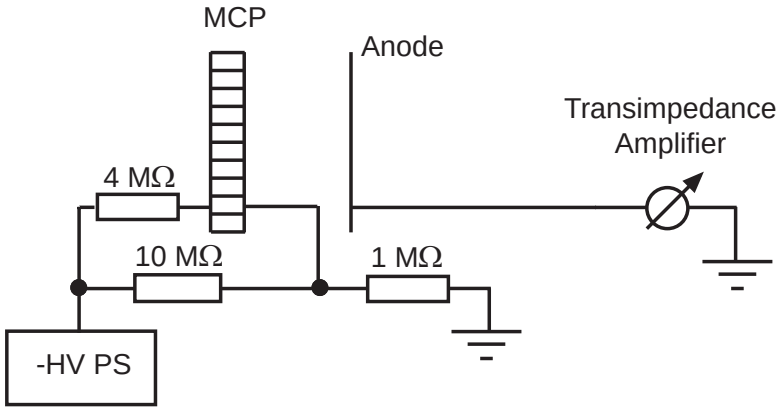


Figure 2.5: MCP power and detection circuit diagram.

means one has to slowly increase the time interval $\Delta t$ after which the magnetic fields are switched off. The synchronous atom will still travel the distance $L$ in the time interval $\Delta t$, but $\phi_0$ will now be different from 0. By definition, the synchronous atom will always be at the same position within a coil, when the magnetic fields are switched off. It can achieve this by losing exactly the required amount of kinetic energy per stage. Again, the atoms that have slightly different phases and velocity from $\phi_0$ and/or $v_0$ will oscillate around those of the decelerated synchronous atom.

The kinetic energy lost by the synchronous atom per stage is given by the potential energy difference $V(\phi_0) - V(\phi_0 - \pi)$. For certain equilibrium phases a well defined region in phase space ($v(\phi)$) will undergo stable phase oscillation. For further detail the reader may refer to reference [20].

However, our apparatus does not provide instant switching which complicates the slowing mechanism. It is, for instance, no longer true that a phase of $\phi_0 = 90°$ provides the highest slowing efficiency although it still holds that it provides the smallest phase space acceptance region. A detailed investigation based on both simulation and experiment will be carried out in the near future. Until then the switching phase can be seen as a free parameter in our setup. Nevertheless some qualitative arguments still hold as can be seen in chapter 4. It should also be mentioned that due to the finite switching time, phases used in our setup are in general much smaller that those commonly used in Stark decelerators.

## 2.3 Beam Detection

Within our time of flight setup we detect the metastable neon using a micro channel plate (MCP) made by El Mul Technologies, Ltd.. An MCP is an array of electron multiplier tubes. When a metastable neon atom hits its surface a free electron is created as the ionization energy of the MCP coating is lower than the excitation energy of the metastable neon (Penning ionization). The created electron is then accelerated towards the surface of the electron multiplier tube by a high voltage gradient. The impact creates secondary electrons which are accelerated again. The created electron avalanche results in a detectable current. Using a low noise adjustable power supply [22] we can vary the MCP's gain between $10^3$ to $10^9$. A circuit diagram is presented in figure 2.5. The signal then is amplified by an SRS voltage amplifier [23] in the case of 18 slowing stages. For the 64 slowing stages a current amplifier [24] is employed. The data acquisition is carried out by a National Instruments Card [25].

# Chapter 3

# Monte Carlo Beam Simulations

Before setting up a pulsed magnetic field slowing apparatus Monte Carlo beam simulations were performed to investigate the feasibility of the slowing scheme. Molecular oxygen was chosen for these simulations as it is one of the few paramagnetic molecules and can be easily seeded into our supersonic beam. Besides pulsed magnetic slowing the idea of a fast moving trap was investigated. The presented simulations have been published in [26].

## 3.1 Pulsed Magnetic Slowing

Molecular oxygen is one of a few molecules that have a permanent magnetic moment in the ground state. It can be introduced into the supersonic beam by mixing it with a heavier carrier gas such as Xenon. The ground electronic state of molecular oxygen is a paramagnetic triplet ($S = 1$) state, $^3\Sigma_g^+$. High intensity magnetic fields split the ground state oxygen into the three magnetic sub-level states with spin projections $M_s = 1$, 0 and $-1$ (within Paschen-Back approximation). The low field seeker, $M_s = 1$, atoms are slowed by the pulsed magnetic fields while $M_s = 0$ atoms remain unaffected and $M_s = -1$ atoms are defocused.

To simulate the slowing of molecular oxygen, we numerically integrate the classical equations of motion using magnetic fields obtained via finite element analysis. These fields are calculated by solving the non-linear magnetostatic equations. We use the coil dimensions shown in figure 4.1 and a current density of $1 \times 10^9\,\mathrm{A/m^2}$. Under the adiabatic approximation the atomic magnetic polarization follows the lo-

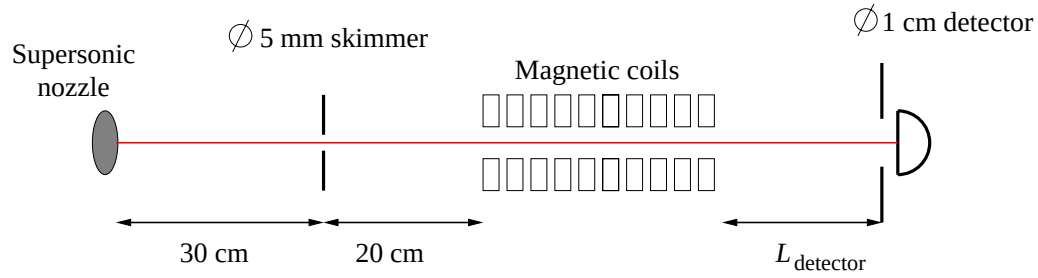


Figure 3.1: A schematic drawing of the magnetic slowing apparatus; the distance between the last coil and the detector, $L_{detector}$ is varied according to the number of employed coils.

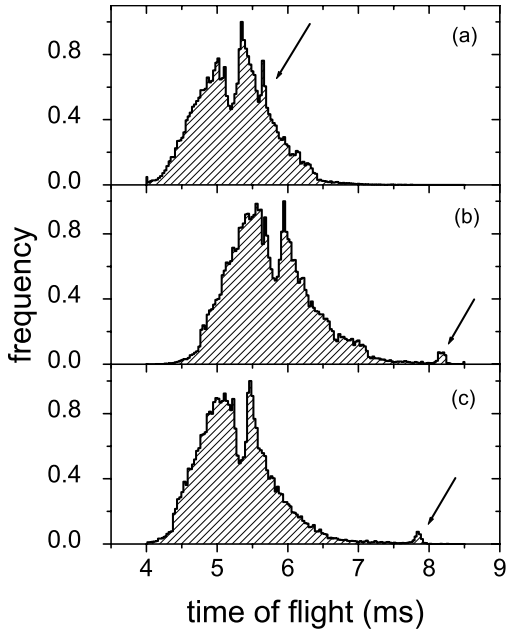


Figure 3.2: The results of time of flight simulations for (a) 20, (b) 48 and (c) 54 slowing coils. The arrow indicates the slowed atoms

cal magnetic field direction and the classical equations of motion can be expressed

as

$$m\ddot{x} = -\frac{\partial}{\partial x}\Delta E \tag{3.1}$$

$$m\ddot{z} = -\frac{\partial}{\partial z}\Delta E \tag{3.2}$$

where $m$ is the oxygen molecular mass, $x$ and $z$ are the transverse and the propagation directions, respectively, and $\Delta E$ is the Zeeman energy shift. We model the electromagnetic coil switching as an exponential function having a time constant of 7 $\mu$s. We model only the switching off of the magnetic field since our simulations start with all the coils being switched on. The simulated oxygen beam has an initial mean velocity of 250 m/s with a standard deviation of 25 m/s. Our simulations only include those atoms within two standard deviations of the mean velocity. The standard deviation of the beam divergence angle is 0.1 rad and the nozzle opening time is taken to be 15 $\mu$s.

A schematic drawing of our simulated magnetic slower setup is presented in figure 3.1. The distance between the supersonic nozzle and the first coil is 0.5 m, the distance between coils (center-to-center) is 14.1 mm, and the distance from the last coil to the detector is 0.5 m, 0.25 m, and 0.05 m for 20, 48 and 54 coils respectively. We choose the timing of our coils such that the molecules with an initial velocity of 250 m/s lose the largest amount of kinetic energy per stage and are thus slowed the most effectively. We present the calculated arrival time distributions at the 1 cm diameter detector in figure 3.2. The plots include arrival time calculations for all three possible $M_s$ states and show that the mean velocity of oxygen can be reduced to 50 m/s after 54 slowing stages. The effective slowing is limited to the molecules that are within $\pm 2$ m/s of the mean velocity and only about 1 % of the detected molecules are slowed.

## 3.2 Moving Trap

In principle, a pulsed magnetic decelerator is able to stop the atomic beam and enable atom transfer into a magnetic trap. A similar process has been demonstrated to produce electrostatically trapped polar molecules [27]. This trapping technique is a two-stage process that requires deceleration before trapping.

We propose to combine trapping with deceleration. Cold and fast atoms

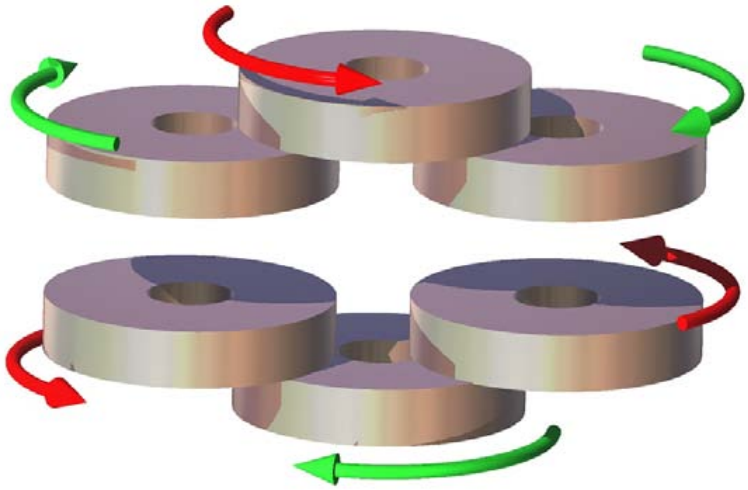

Figure 3.3: Schematic drawing of three anti-Helmholtz coil pairs that are sequentially activated to create a moving magnetic trap. The direction of the current in each coil is represented by an arrow. The coil dimensions are: 9 mm diameter, 1 mm height and 3 mm bore. The left and right anti-Helmholtz coil pairs are separated by 3 mm whereas the center pair separation is 5 mm. The maximal current flowing through the coils is 200 A for the left and right coils and 400 A for the center ones.

from the supersonic beam would be trapped in a co-moving, decelerating magnetic trap. The initial trap velocity is equal to the atomic beam velocity. Since the beam temperature in the moving frame is very low (under 100 mK), we can trap a large number of atoms. The number of atoms that 'survive' the slowing process depends on the deceleration value.

Our proposed electromagnetic coil configuration for the adiabatic slowing process (see figure 3.3) is similar to the set-up used by Greiner et al. [28] to transfer laser-cooled atoms over macroscopic distances. In our case the unit cell consists of three anti-Helmholtz coil pairs that create a moving 1 $mm^3$, 0.4 T deep magnetic trap. The magnetic field minimum can be translated by changing the current ratio between two of the anti-Helmholtz coil pairs.

We simulate the adiabatic slowing process for the case of $M_s = +1$ state of molecular oxygen. We use the same supersonic beam properties as in the previous section; however, our calculations here are one-dimensional (1D). We switch the magnetic trap around the atoms instantaneously and slow it down with a constant

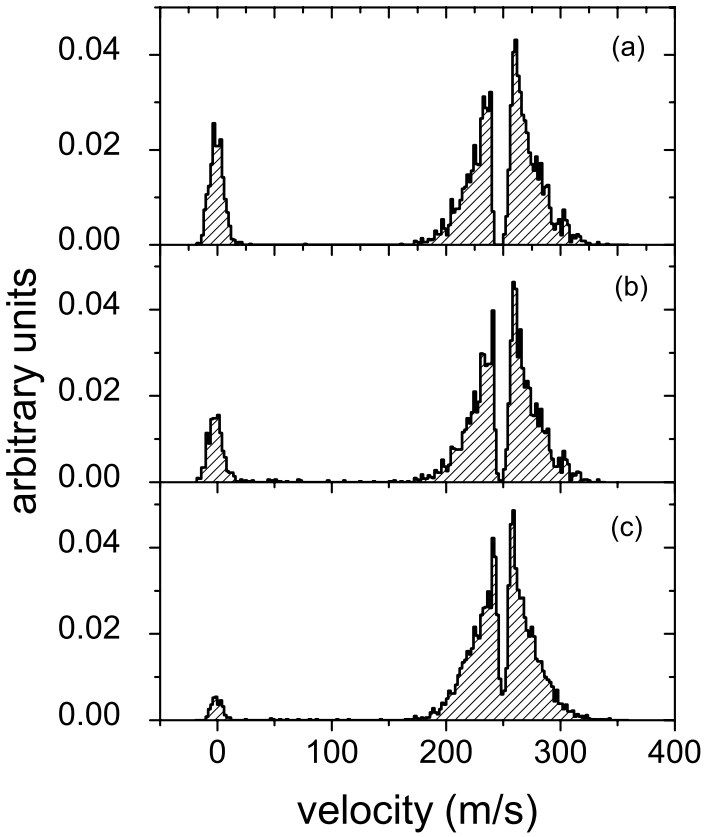


Figure 3.4: Simulated velocity distributions of adiabatically stopped $O_2$ molecules in the $M_s = 1$ state. The acceleration values are (a) $-4 \times 10^3\,\mathrm{ms}^{-2}$, (b) $-1 \times 10^4\,\mathrm{ms}^{-2}$, and (c) $-4 \times 10^4\,\mathrm{ms}^{-2}$.

deceleration. The resulting velocity distributions are shown in figure 3.4. As expected, the number of slowed molecules depends on the deceleration. The trapping efficiency is about 5 % in the case of the largest acceleration of $-40,000\,\mathrm{ms}^{-2}$. The total length of such an adiabatic decelerator device would be about 80 cm.

# Chapter 4

# 18 Stage Magnetic Slower

In this chapter we describe the first generation of a pulsed magnetic slower with 18 stages which has been published in [29]. The system was designed to show that magnetic slowing works in principal and to gain experience in building coils and driver circuits. We give a detailed description of the coil assembly, the vacuum system, and the driver circuit before we characterize our magnetic fields and explain the pulse generation.

In the results section 4.2 we present time of flight measurements of metastable neon which we slow from 460 m/s to 400 m/s resulting in a peak in the time of flight measurement that is clearly separated from the initial distribution.

## 4.1 Setup

In the following section we describe the design of the 18 stage magnetic slower. It was originally designed as a 20 stage device but the wires in coils 17 and 19 shorted to ground, and thus rendered these stages inoperable.

### 4.1.1 Coil Assembly

A schematic of the electromagnetic coil assembly is shown in figure 4.1. This design is inspired by the coil used to open the supersonic nozzle (see section 2.1.1). The $5\times6$ copper windings are wound around a hollow vespel cylinder with a wall thickness of 50 $\mu$m. This cylinder keeps the kapton and permendur discs at the right distance during the winding process during which these five parts are clamped onto a screw-

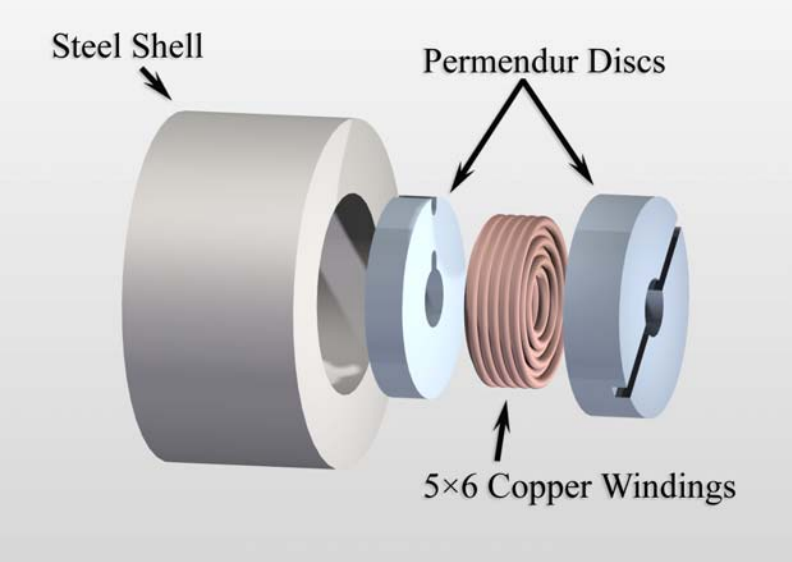


Figure 4.1: A schematic blow up of our electromagnetic coils. The bore diameter is 3 mm and the axial length is also 3 mm.

like winding tool. The kapton discs prevent the wire, a 500 $\mu$m coil wire with 25 $\mu$m of kapton insulation, from being scratched during the winding process. As a further protection, the wire is covered with teflon heat shrink tubing with a wall thickness of 152 $\mu$m where it enters and exits the metal enclosure. The permendur disc with the wire outlet slots has a thickness of 2.5 mm, the one that is screwed onto the magnetic steel shell is 3 mm thick. As the steel shell has a 0.5 mm thick bottom one finds 3 mm shielding material on each side of the copper coil. In order to keep the wires in place during the current pulse (attractive forces between to adjacent wires are on the order of 6 N), to avoid virtual leaks and to guarantee an adequate thermal conductivity the empty space within the steel shell is filled with a thermally conductive, UHV compatible epoxy [30].

The steel shell is inserted into a copper disc which guarantees the alignment of all individual coils within the slower. It also enables us to water cool the coils as it is indium soldered to a copper tubing through which we run chilled water. Within the copper disc the steel shell is held in place by a small set screw. The same thread is used to clamp the wire to the disc using a folded piece of Kapton and a vented screw to avoid virtual leaks.

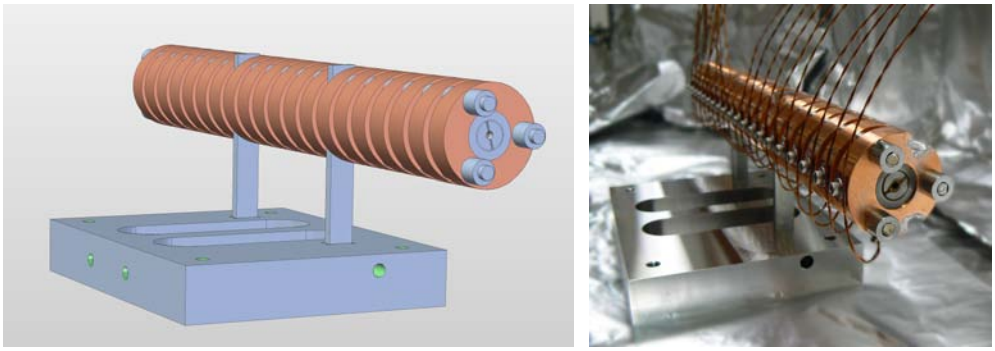

Figure 4.2: Schematic of the magnetic slowing apparatus (*left*) and actual photograph (*right*).

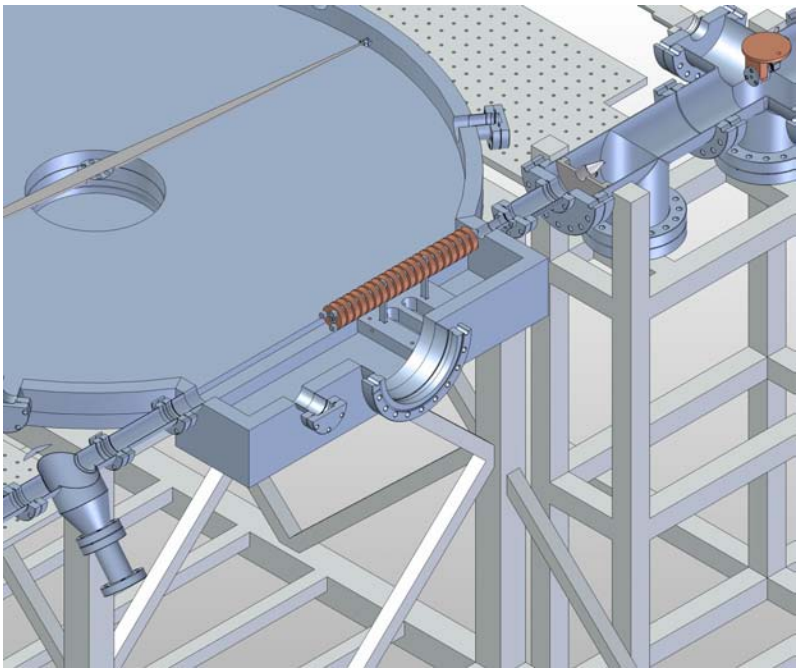

Figure 4.3: CAD drawing of the existing vacuum chamber [13] with the 18 slowing stages. The supersonic beam is generated with the cryogenic valve (*upper right corner*) and passes a skimmer before entering the main chamber. After passing through the slower the beam travels an additional 1.5 m to the MCP detector (not shown).

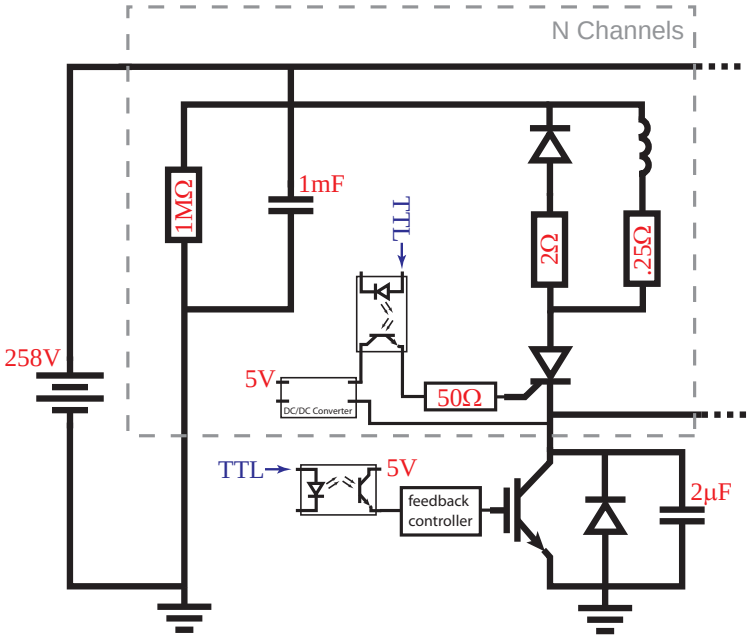


Figure 4.4: Circuit diagram of the coil driver. 2 or 3 of the depicted channels are connected to one IGBT. We used 8 IGBTs for 18 drivers.

Since this slower setup was designed for proof of principle experiments a setup using the already existing vacuum chamber [2] was used. The slower is shown in figure 4.2. The copper discs are stacked onto three stainless steel rods. To achieve a equal spacing, stainless steel spacers are utilized resulting in a center to center distance of two neighboring coils of 14.1 mm. After the seventh and thirteenth coil the spacers are replaced by a post which rises from a stainless steel block that can be height adjusted with set screws. The placement of the slower in the existing vacuum chamber is shown in figure 4.3. After the slower exit the beam travels 1.5 m to the MCP detector which is mounted on a translation stage (also see chapter 5). This stage allows us to move the MCP by 5.08 cm along the beam line. By recording time of flight in both the extended and retracted positions the velocity of any part of the beam can be calculated.

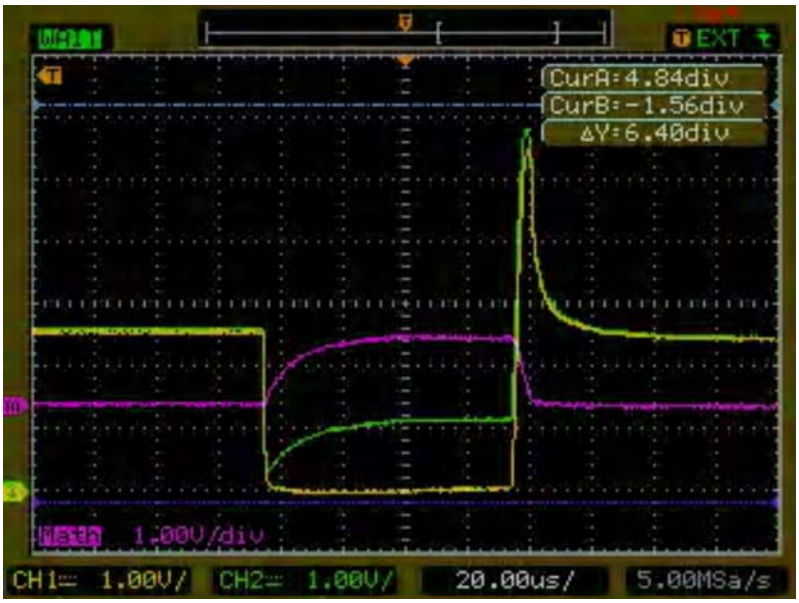


Figure 4.5: This figure shows a typical current evolution in the coil during an 80 $\mu$s capacitor discharge measured over the 0.25 Ω resistor (see figure 4.4) using 1/100 probes. The yellow curve is measured in front of the resistor, the green one after and the pink is the difference, i.e. 1/4 of the current. Although the current drops from 400 A to 0 A within 7 $\mu$s the magnetic field remains at about 20 % of its peak value due to Eddy currents and the hysteresis of permendur (see figure 4.7).

### 4.1.2 Driver Electronics

A schematic of the circuit that drives the electromagnetic coils is shown in figure 4.4. Parts within the grey dashed box exist for each channel, the ones outside are shared.

The left side of figure 4.4 shows the power part of the driving circuit. The 1 mF capacitor is charged by a 258 V power supply (two sets of five switching 50 V power supplies connected in series [31]) with a maximum output of 2.1 A. To discharge the 1 mF capacitor slowly after the power is turned off a 1 MΩ resistor is placed parallel to the capacitor to ground, allowing a discharging time constant of $\tau = 17$ min. This means that the boxes with the driver electronics can be safely opened one hour after the power has been disconnected.

On the right side of figure 4.4 the switching part of the circuit is depicted. The combination of a thyristor and an isolated gate bipolar transistor (IGBT) allows

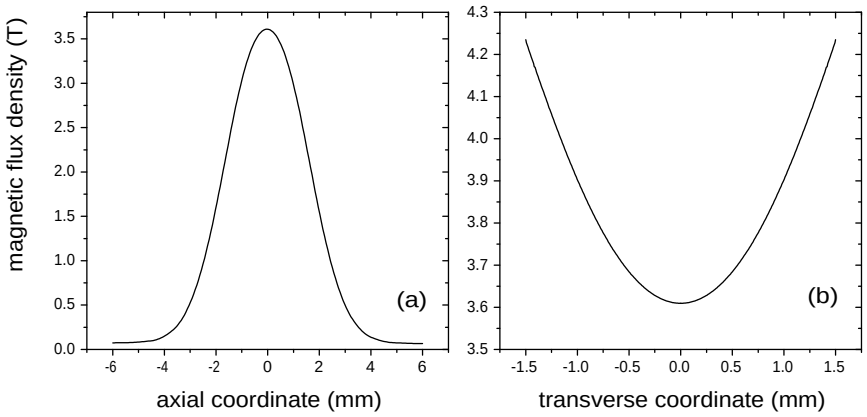


Figure 4.6: Transverse and longitudinal magnetic field profile as simulated via finite element analysis [33] for a current of 400 A within the actual coil geometry.

us to use the well defined switching characteristic of the IGBT [32] to switch off the current for several channels: Opening a thyristor and an IGBT at the same time discharges the 1 mF capacitor. In contrast to the thyristor, the IGBT can be closed actively. If it stays closed for at least 37 $\mu$s the thyristor will be effectively closed and will stay closed until it gets another opening signal at its gate. Using eight IGBTs, applying 80 $\mu$s current pulses to the coil and giving the thyristor a time of 60 $\mu$s to close allows us to fire one IGBT every 140 $\mu$s. Given the distance between nine coils $\Delta z = 8 \cdot 1.41\,\text{cm} = 11.28\,\text{cm}$ we can calculate the maximum velocity that can be slowed with our slower: $v_{max} = 805\,\text{m/s}$. In order to start out with higher velocities a higher number of IGBTs is required.

When two TTL pulses are provided, one to a thyristor rated to $V_{peak} = 600\text{V}$, $I_{peak} = 40\,\text{A}$ DC and one to its corresponding IGBT, the 1 mF capacitor starts discharging through the coil. As the total resistance, consisting of the $0.25\,\Omega$ resistor, coil wire, feedthrough connectors and internal capacitor resistance, is measured to be $R = 0.60\,\Omega$, the applied 258 V leads to a current of $I = 430\,\text{A}$. A typical current profile can be seen in figure 4.5.

When the IGBT is switched off its emitter jumps to $\sim$ 550 V due to the coil's back EMF as the coil tries to maintain the current but the connection to ground is cut. Usually in this situation the emitter voltage would oscillate but these oscillations are damped by a small snubber capacitor (2 $\mu$F) which is connected

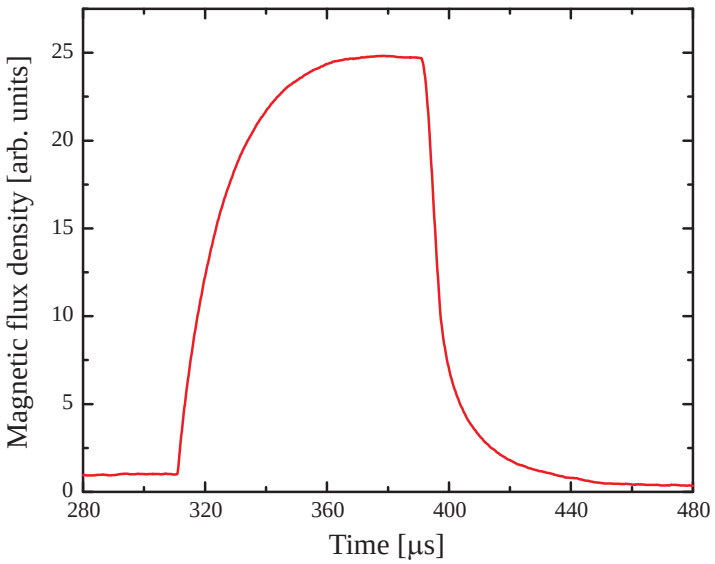


Figure 4.7: Qualitative time profile of the magnetic flux density in the center of the coil. Shown is the numerical integration of the current induced in a small pickup coil placed in the center of the slowing solenoid. After the 80 $\mu$s current pulse is switched off the field falls linearly to about 20 % of its peak value and decays then exponentially.

across the IGBT. In order to keep the voltage jump below the peak voltage rating of the IGBTs (600 V) a 2 Ω resistor is connected in parallel to the coil. When the 1 mF capacitor discharges this path is blocked by a diode but it allows current to flow back into the big capacitor without passing the coil. This technique helps to control the voltage jump but also lengthens the time the field in the coil takes to decay. This can easily be understood if one sees the voltage jump as a counter pulse that drives the coil in reverse [34].

As the thyristor needs a current of 20 mA flowing from its gate to its cathode to open, a positive voltage relative to its cathode must be applied to its gate. In order to achieve that a DC/DC converter is used. The 50 Ω resistor limits the current to the required 20 mA, the opto-coupler protects the digital signal source by physically disconnecting it from the high voltage circuit.

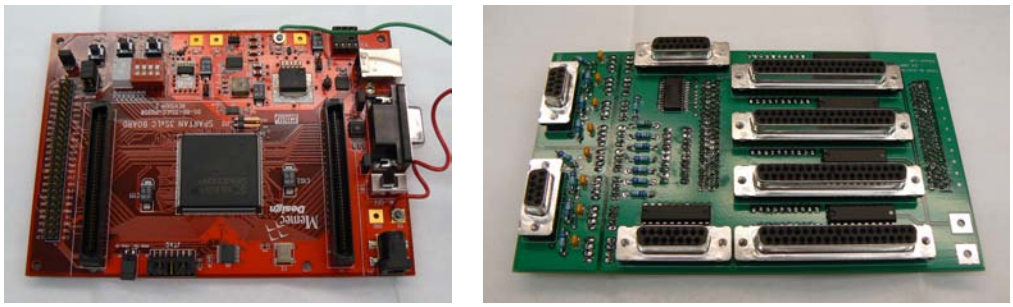

Figure 4.8: *Left:* Picture of the used FPGA [35]. *Right:* Picture of the home-built buffer and distributor board

### 4.1.3 Magnetic Field Characteristics

The magnetic flux density profile as expected from finite element analysis is shown in figure 4.6. A current of 400 A flowing through our coils creates a magnetic field of 3.6 T at the center of the coil. The almost harmonic radial profile guides atoms in the low field seeking state through the slower whereas high field seekers are scattered out of the beam.

The time evolution of the magnetic field as measured with a pickup coil in the center of the solenoid is depicted in figure 4.7. Shown is the numerical integration of the current induced in an ungauged pickup coil. The lack of calibration here makes statements about the absolute field values impossible. Nevertheless, one can see that the field rises slowly during the applied 80 $\mu$s current pulse, drops linearly to about 20 % of its peak value within the first 7 $\mu$s after the current is turned off, and decays then exponentially.

### 4.1.4 Pulse Generation

The timing of the coils is a crucial part of the magnetic slowing experiment. Driving 18 slowing stages, i.e. 18 thyristors and 8 IGBTs, as well as the pulsed nozzle and discharge in sync requires more than 30 digital counters. Low tolerances in timing make a hardware solution preferable. A cheap and fairly simple way of implementation is offered by field programmable gate arrays (FPGA).

We use a Spartan 3SxLC by Xilinx [35] with 140 digital outputs and an external clock of 10 MHz allowing a time resolution of 100 ns. The two JX outputs of the FPGA are buffered and distributed over D-Sub connectors using a self-made

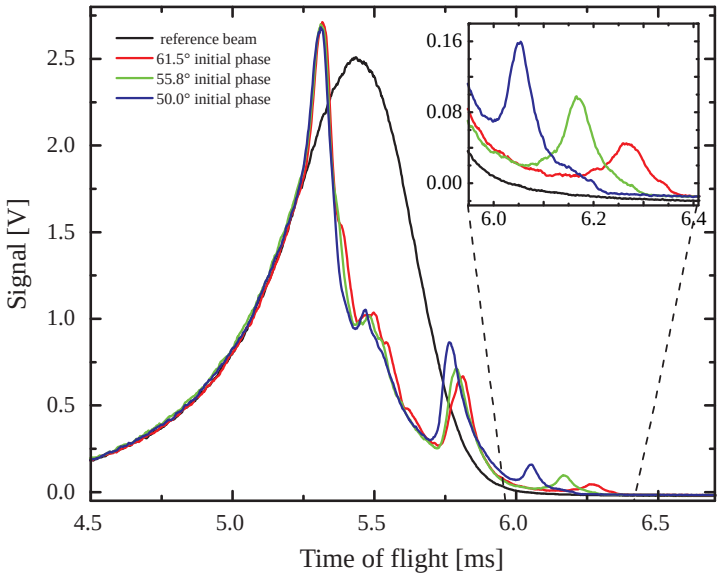


Figure 4.9: A plot of the arrival time of metastable neon atoms at our MCP detector, with varied switching phases. Each curve is an average over 10 shots, at a current of 400 A and a repetition rate of 0.2 Hz. The reference beam is the beam detected without pulsing the coils. Here, a larger phase angle leads to greater slowing, but a smaller region of phase stability. The slowed peaks are seen at the right side of the graph, and in the expanded inset.

distributor board (see figure 4.8). Each channel but the discharge is connected through an opto-coupler to the TTL receiving component in order to protect the logic circuit from overvoltages that might occur on the analog side.

## 4.2 Results

We now present time of flight results for metastable neon, varying the phase of the switching in figure 4.9, along with a comparison reference beam. The phase is adjusted linearly with velocity. To determine the position of the slowed peak we use a MatLab routine that fits one exponential and two Gaussians in the estimated region of the slowed peak, taking the exponential tail of the original distribution and the slow beam shape into account. We use phase angles of 50.0°, 55.8°, and 61.5° (final phase angles are 51.5°, 58.7°, and 64.3°, respectively) to demonstrate

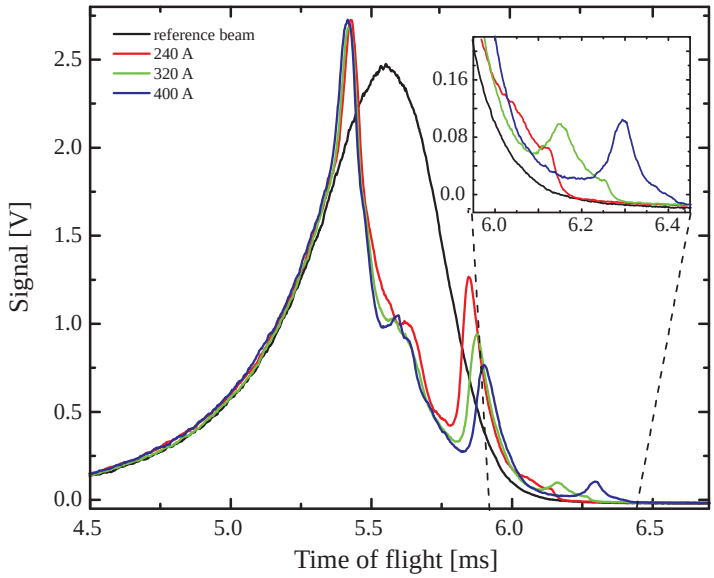


Figure 4.10: A plot of arrival time at the MCP detector, with varied currents in the coils. Each curve is an average over 10 shots, using a phase angle of 11.3° and a repetition rate of 0.2 Hz. The higher currents lead to greater magnetic fields and thus more slowing. The slowed peaks are on the right side of the graph, and in the expanded inset.

the difference in slowing due to a variation in phase angle, as well as changes in flux. Using the translation stage as described in subsection 4.1.1, we calculate speeds of $431.2 \pm 6.0$ m/s, $409.3 \pm 9.1$ m/s, and $403 \pm 16$ m/s, corresponding to a slowing of 30 m/s, 52 m/s, and 58 m/s from the original 461 m/s. Setting a phase angle of 61.5°, we find that our slower removes a kinetic energy of 0.288 meV ($2.33\ \mathrm{cm}^{-1}$) per stage.

To examine the effects of magnetic field strength, we vary the current in the coils. The currents we use are 400 A, 320 A, and 240 A as currents lower than this do not separate the slowed peak from the main beam. These currents correspond to maximum magnetic field densities of 3.6 T, 3 T, and 2.4 T. As can be seen in figure 4.10, we see less slowing for lower fields. The corresponding velocities, as calculated by the translation stage, for these currents are $409.3 \pm 9.1$ m/s, and $416 \pm 22$ m/s for 400 A and 320 A respectively. We are not able to definitively determine the velocity for 240 A as the peak is not resolved.

Comparing the resulting beam shape to the reference beam in figures 4.9 and 4.10 we observe that the original beam is greatly disturbed by the pulsing of the coils. We explain the shape of the resulting beam qualitatively. The metastable atoms in the reference beam do not all have the same angular momentum projections, and while our coils focus low field seekers, the high field seekers are defocused, leading to a loss of atoms compared to the reference beam. While this explains the minimum seen in the plots, we must still address the two peaks seen on either side of this minimum. These occur because not all atoms that feel the pulses of the field are slowed. Some atoms will be accelerated slightly by one or two coils before falling out of sync with the pulses, which produces the peak leading the minimum. The peak trailing the minimum can be explained in the same manner, except that the atoms are slowed slightly instead of accelerated.

# Chapter 5

# 64 Stage Magnetic Slower

In this chapter we describe our second generation pulsed magnetic slower. It consists of 64 stages and major improvements in the driver circuit allow significantly higher slowing than the 18 stage model. We again describe the coil assembly, the vacuum chamber, and the driver electronics in detail. A thorough characterization of the generated magnetic fields follows. Finally, some preliminary results are presented demonstrating the slowing of metastable neon from 443 m/s to 136 m/s and revealing a strong flux dependence on the slowing phase.

## 5.1 Setup

### 5.1.1 Coil Assembly

There are two main problems with the coil design of the 18 stage slower (see chapter 4): The steel cup takes a lot of machining time since it needs to have a flat bottom, which can not be achieved by simple drilling. The second problem arises winding the coils as the wire is scratched when it is bent by 90° to fit the outer notch that allows the wire to exit the metal case.

The new design (see figure 5.1) takes care of both problems. The magnetic steel cup is replaced by a steel tube with a standard size bore. As the permendur discs are glued in place the process of cutting a thread is also superfluous. The long cut in the steel tube allows the wire to exit the metal shell in a straight way decreasing the risk of cutting the insulation to a minimum. In addition, all possibly sharp edges on the permendur discs as well as the steel tube are de-burred. However,

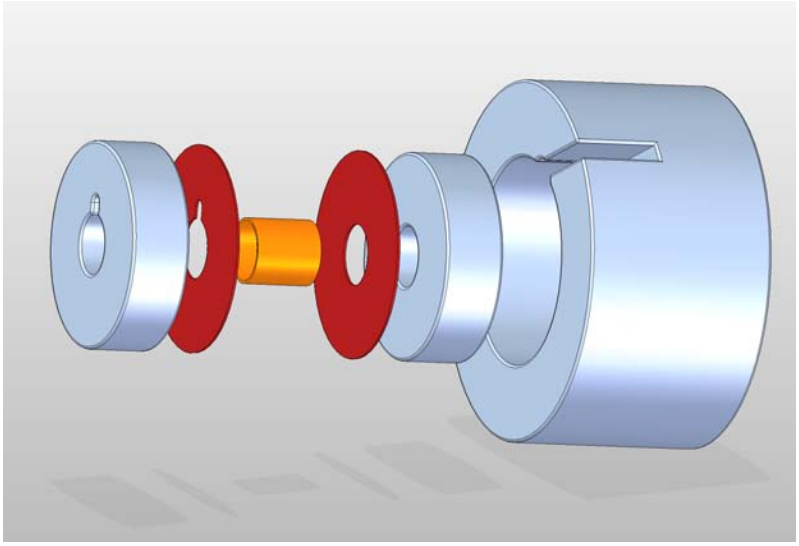

Figure 5.1: Schematic of the coil design for the 64 stage magnetic slower. The $5 \times 6$ copper windings (*not shown*) are wound around a thin wall vespel cylinder (*orange*) and protected against scratches from the permendur [17] discs (*grey*) by kapton washers (*red*). This whole inner part is then glued with UHV epoxy into the outer magnetic steel shell.

since this design is no longer closed by a threaded cap a mold must be used to align the parts during the gluing process. We use two teflon plates with c-clamps. A groove in one of the plates allows extra epoxy to escape from the coil creating a lip witch serves as an additional wire protection. To prevent the epoxy from flowing into the coil bore it is filled with a teflon rod. After the epoxy is cured by baking it for 3 hours at 150°C the extra epoxy is removed with sandpaper. A picture sequence of the gluing process is provided in figure 5.2.

We use the same wire as in chapter 4, a 500 $\mu$m coil wire with a 25 $\mu$m kapton insulation. It is wound in 6 layers each with 5 turns around the vespel cylinder (wall thickness of 100 $\mu$m) and in between two kapton washers (thickness of 150 $\mu$m) to avoid direct contact to the permendur discs. The discs are 3 mm thick. After the winding the coil is transfered from the winding tool onto a teflon rod with a diameter of 3 mm corresponding to the coil bore size. The rod is stuck in a teflon mold providing a groove that creates an epoxy support for the wire exiting the metal enclosure (see figure 5.2(a)). After the transfer the upper permendur disc

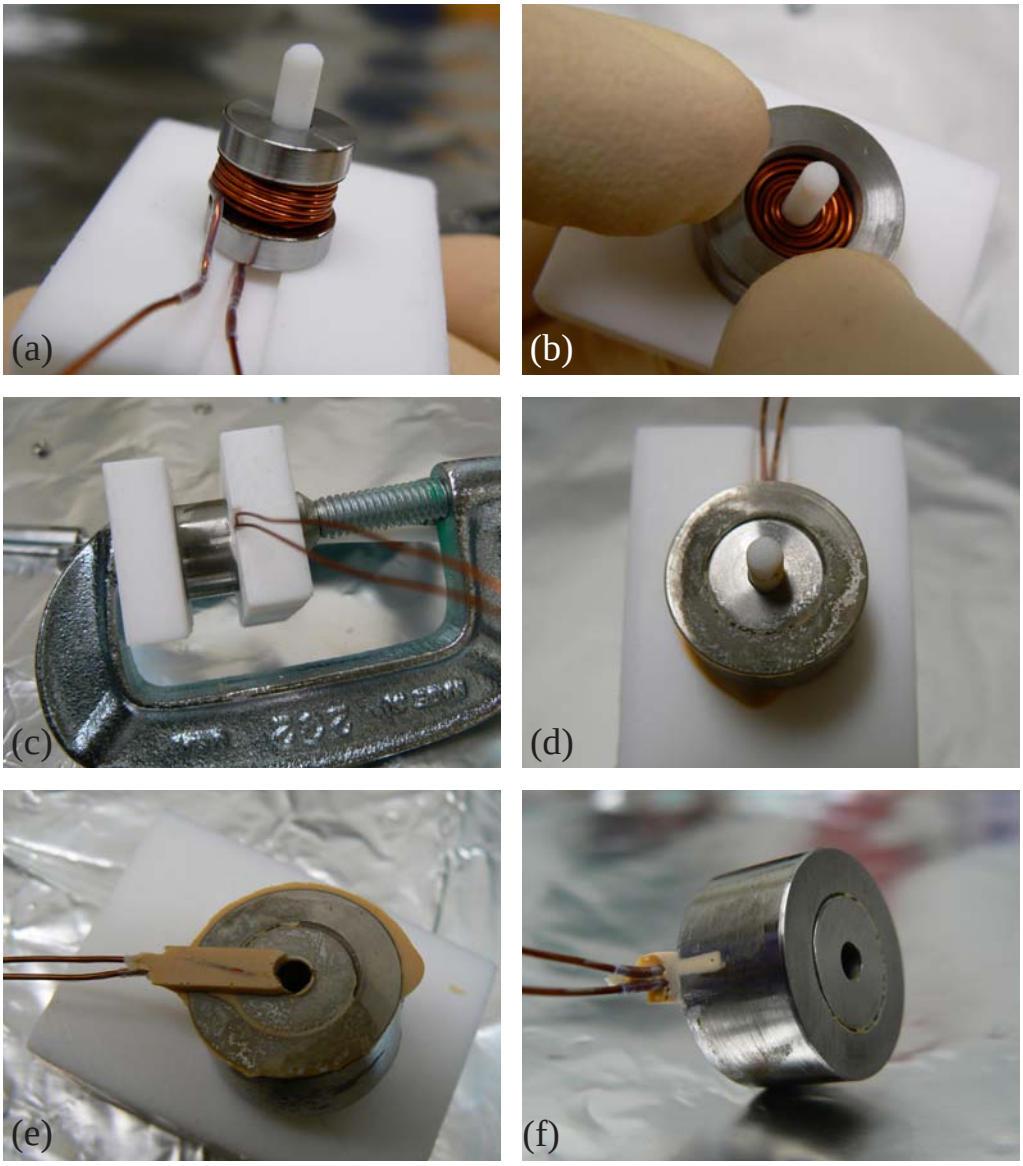


Figure 5.2: Overview of the gluing process. (a) Shown is the actual coil sandwiched between the kapton and permendur discs. One can see the groove in the teflon mold forming the epoxy lip that guides the wire. (b) The top kapton washer and permendur disk are removed to fill in the epoxy. (c) Coil with uncured epoxy between teflon molds held by a c-clamp. (d) Top view of the readily glued coil. (e) Detail of the epoxy lip. Before the coil can be used the extra epoxy must be sanded of. (f) The coil is done.

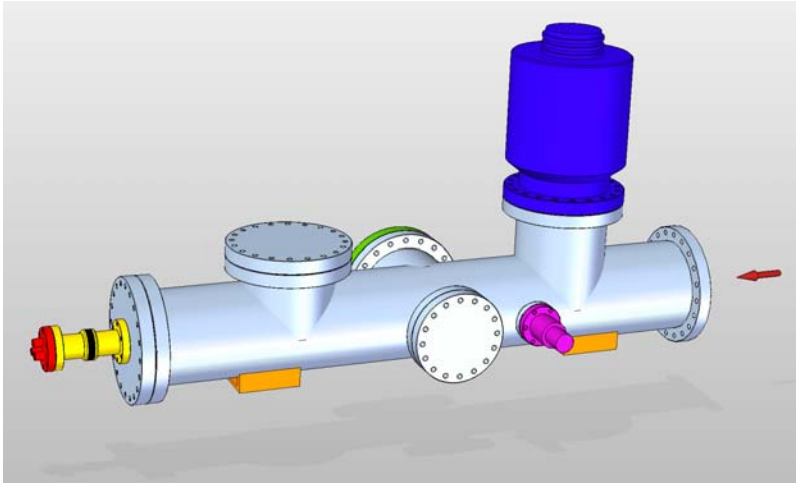

Figure 5.3: CAD drawing of the vacuum chamber. The beam path is indicated by the red arrow. The slower is placed in a 6 in tube (figure 5.4) kept from rotation by two welded feet (*orange*). We use a 551 l/s turbomolecular pump (*blue*) to pump the chamber to $1 \times 10^{-8}$ tor measured by a cold cathode ion gauge (*pink*). Wires to power the coils are connected through an 8 in flange with 3 50-pin D-Sub connectors (*green*). The MCP detector is mounted on a feedthrough flange (*red*) which can be translated by 5.08 cm using edge-welded bellows (*yellow*) which are shown in the retracted position.

and kapton washer are removed. With the magnetic steel tube placed around the coil epoxy [30] is applied to the upper coil windings using a custom built teflon spatula (figure 5.2(b)). The epoxy is very viscous at room temperature, but heating it carefully to 50°C causes it to flow. Shaking and knocking the coil assembly softly spreads the epoxy well. When enough epoxy is applied the coil is closed with the top kapton and permendur discs and clamped with another teflon piece using a c-clamp (figure 5.2(c)). After curing the glue for 3 h at 150°C the clamps can be taken off (figure 5.2(d),(e)). Excess epoxy can be removed with a pair of pliers and sandpaper. The finished coil is shown in figure 5.2(f).

### 5.1.2 Vacuum Chamber and Coil Mount

A CAD drawing of our vacuum chamber is presented in figure 5.3. The beam propagation direction is indicated by the red arrow. The chamber consists of a single 6 in stainless steel tube ensuring straightness. Three 8 in, one 6 in, and one

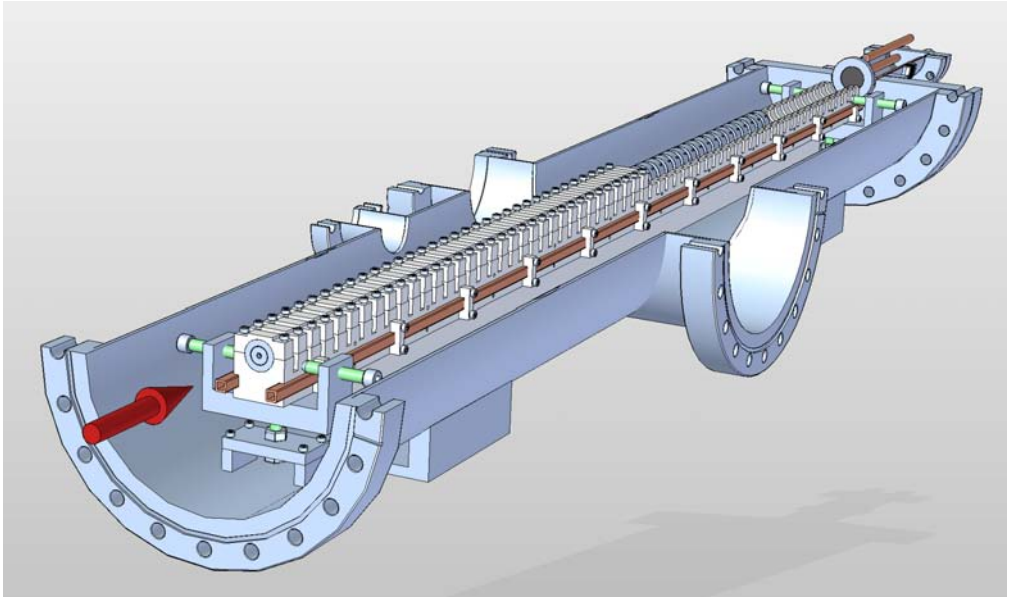

Figure 5.4: CAD drawing of the inside of the vacuum chamber. Again, the red arrow indicates the beam path. Only the first 49 coils and 32 clamps are shown to clear the view of the detector. The MCP is mounted on three copper rods to minimize distance of flight. A square copper tube is clamped onto the aluminum piece holding the coils allowing to watercool the system.

2 3/4 in flanges are branching off. All flanges are ConFlat. The chamber is mounted using the welded feet (*orange*) onto an aluminum support structure (*not depicted*).

The chamber is kept at a pressure of $1 \times 10^{-8}$ tor by a 55 l/s turbomolecular pump (*blue*) [36]. The pressure is measured with a cold cathode gauge (*pink*) [37]. The 64 wire pairs powering the coils are connected through an 8 in blank with three 50-pin D-Sub connectors (*green*) [38]. The 2 3/4 in blank holding the MCP detector (*red*, also see figure 5.4) is outfitted for that purpose with three MHV feedthroughs. It itself is mounted onto welded bellows (*yellow*) which allow us to move the detector by 50.8 mm along the beam axis. Shown are the bellows in the retracted position. As the bellows are not stiff enough to resist bending due to gravity they are supported by an aluminum translation stage (*not shown*).

The inside of the vacuum chamber is shown in figure 5.4. The coils are mounted with a center to center distance of 14.1 mm onto a single aluminum piece ensuring axial alignment within 50 $\mu$m. A fin on the bottom adds additional stiffness

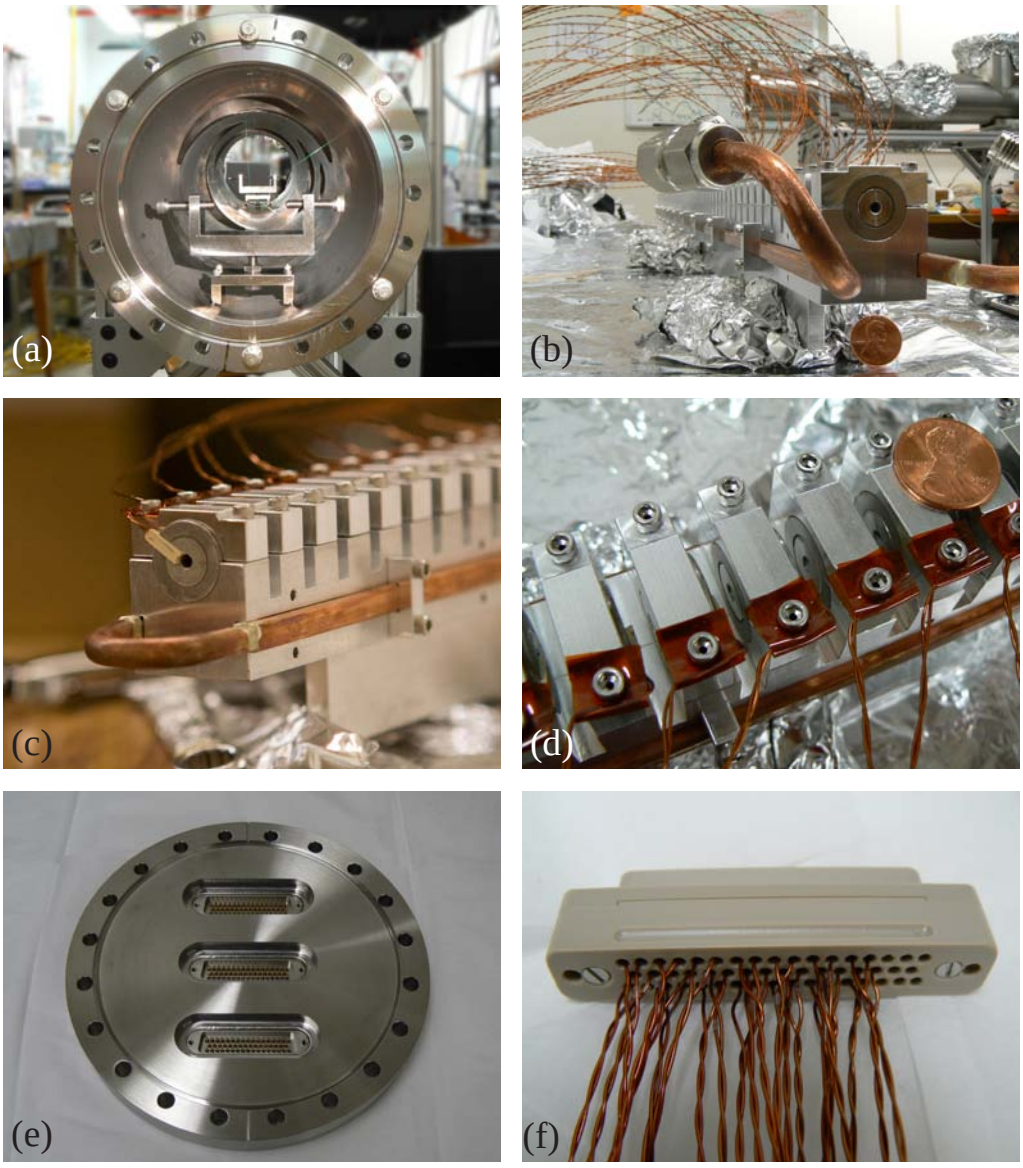


Figure 5.5: Detail views of the 64 stage magnetic slower. (a) View of the 6in vacuum tube with the translation stage and cross hairs. (b) The entrance of the slower. The copper horn in the front allows to attach watercooling. (c) Exit of the slower. (d) The wires energizing the coils are fixed using a folded piece of kapton. (e) Electrical feedthrough blank. (f) Vacuum side 50 pin D-Sub PEEK connector with coil wires.

to the support, ensuring a beam deflection of less than 100 $\mu$m. Each coil is clamped down individually into a half circular groove by an aluminum clamp. This system allows the replacement of individual coils if necessary. The wires are fixed with a folded piece of kapton on one of the vented screws that hold down the aluminum clamp (see figure 5.5(d)) to make sure that during a rework process no tearing forces are applied onto the wire outlet of the coil. To bundle and protect the wires between the aluminum and the PEEK D-Sub connector they are wrapped with a PEEK spiral. The connection between vacuum side and air side is established using an 8in blank with three 50 pin D-Sub feedthroughs (see figure 5.5(e)). The aluminum structure is watercooled through a 1/4 in square copper tube. To run it back and forth along the aluminum two straight pieces are connected with a u-shaped round copper tube silver soldered to the square tube. The face touching the aluminum structure is polished and the tube is clamped to the structure every sixth coil as illustrated in figure 5.4.

The 89.77 cm long aluminum support sits on two translation stages which allow adjustment in height using the threaded stand as well as vertical adjustment using two 1/4-20 screws with rounded tips. For the latter purpose the aluminum piece slides on the translation stage. We align the coils to crosshairs on both ends of the 6 in tube using a telescope and lock down the aluminum support. Alignment of the nozzle with the slowing stages is then accomplished using a telescope again by moving the nozzle chamber.

On the exit of the slowing tube we mount our MCP detector using welded bellows [39] that allow a translation of 50.8 mm along the beam line. This allows us to determine the velocity of the beam: Recording time of flight data in both the retracted and extended position reveals the time atoms need to travel 50.8 mm translating directly to a velocity. As the welded bellows are quite lengthy we mount our MCP detector on 1/4 in thick copper rods to shorten the distance of flight from the slower exit to the detector to 4 cm (9.08 cm) in the retracted (extended) position. A short distance of flight after the slower is desirable since the longitudinal velocity of the beam is significantly reduced whereas the radial velocity is slightly increased resulting in a beam with a strong divergence.

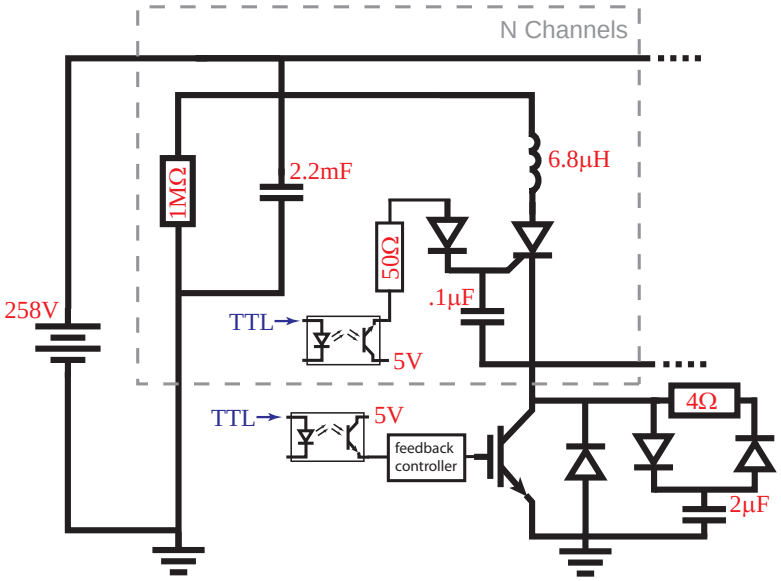


Figure 5.6: Circuit diagram of the coil driver. 8 of the depicted channels are connected to one IGBT. Using 8 IGBTs results in 64 drivers.

### 5.1.3 Driver Electronics

A schematic of the driver circuit is shown in figure 5.6. The power circuit as well as the main idea of using only 8 IGBTs remain the same as described in section 4.1.2. However, changing the IGBTs [40] to a model that can take higher peak voltages (up to 1.2 kV), allows us to drive the coil at a higher current. To achieve this we remove the 0.25 Ω resistor so that the new total resistance is measured to be $R = 0.35\,\Omega$, the applied 258 V leads to a current of $I = 740$ A. Almost doubling the current causes a faster discharge of the capacitor. In addition, a more sophisticated system of measuring the magnetic fields (see following section) reveals that current pulses of 100 $\mu$s are preferable to 80 $\mu$s as the field rises slower than the current profile. For both of these reasons we replace the 1 mF capacitor with a 2.2 mF model.

Driving higher currents and removing the 2 Ω resistor that was parallel to the coil creates a voltage jump of almost 1000 V when the IGBT switches off, which is favorable since it creates a current couterpulse which helps to switch off the magnetic field faster. We also switch to thyristors with a rating of maximum 1000 V and 55 A. Since DC/DC converters for these high voltages are expensive we take

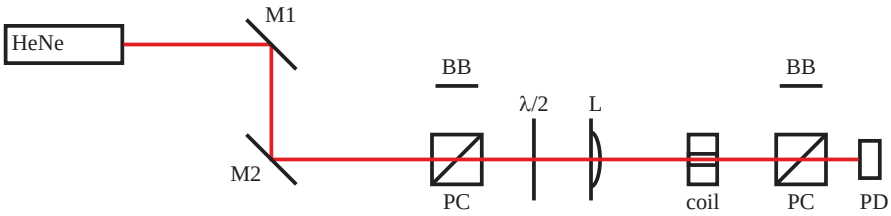


Figure 5.7: Schematic of the coil characterization setup. M1 and M2 are mirrors to level the beam path. The Beam passes a polarizing cube (PC) and a $\lambda/2$-plate and is focused by a 83 mm lens (L) into the TGG crystal inside the coil. The beam is detected using a photo diode (PD) after an analysis polarizing cube. Scattered light is blocked by two beam blocks (BB).

them out of the circuit and connect the gate of the thyristor through a diode and a current limiting resistor to the 5 V line. The trigger is still provided through an opto-coupler. The diode is rated to 2 kV and protects the opto-coupler against the voltage spike. Since the thyristor needs a 5 V signal relative to its cathode to open we need to pin the cathode to ground before we can apply the thyristor pulse. That can be accomplished by opening the IGBT earlier than the thyristor. We choose to open the IGBT 20 $\mu$s prior to the thyristor pulse. This allows the 2 $\mu$F snubber capacitor to discharge completely. To damp oscillations that occur if this capacitor is just shorted to ground we connect a 4 $\Omega$ resistor between the snubber capacitor and ground. The two opposing diodes allow a small charging resistance at the same time.

### 5.1.4 Magnetic Field Characteristics

#### Setup

We use the Faraday effect as described in section 2.2.3 to characterize our magnetic fields. The setup used to characterize the magnetic field produced by our coils is shown in figure 5.7. A linearly polarized Helium-Neon laser beam passes through a 0.5in polarizing cube before hitting a $\lambda/2$-plate which provides a means to rotate the polarization plane. The beam is then focused down with a 83 mm-lens to a spot size of 80 $\mu$m ($2\sigma$-waist $w = 40\,\mu$m). The electromagnetic coil is placed with its center in the lens's focus and a terbium gallium garnet crystal is inserted into its bore. Three crystals [19] with a diameter of 3 mm and lengths of 1.4, 1.5, and 5 mm are available.

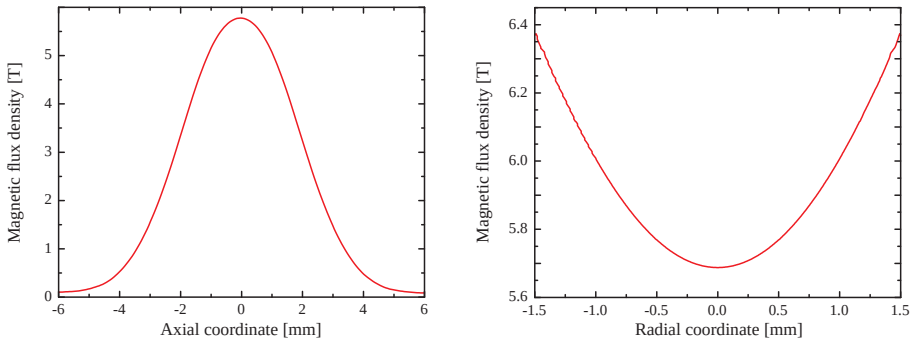


Figure 5.8: Transverse and longitudinal magnetic field profile as simulated via finite element analysis [33] for a current of 740 A within the actual coil geometry.

Before hitting a photodiode the beam passes through another polarizing cube. The photo current is then amplified with a transimpedance amplifier [24] and recorded with the National Instruments card in the case of absolute field measurements, and with a 100 MHz oscilloscope [41] in the case of time profile measurements as it provides a higher sampling rate.

Since the crystals have a finite length and the field has a strong spatial dependence (see figure 5.8) the measurement returns the integral over the $B$-field profile along the beam propagation axis. The integration in the transverse direction can be neglected because of the tight spot size. In addition, the arrangement of polarizing elements leads to a cosine squared dependence of the intensity on the rotation angle so that the detected signal yields the following relation

$$\frac{I}{I_0} = \cos^2\left[\int_{-d/2}^{d/2} dz\, V B(z)\right] \tag{5.1}$$

where $I_0$ is the maximum light intensity, $d$ is the crystal thickness, $B(z)$ the magnetic field along the coil axis and $V$ the crystal's Verdet constant (see equation (2.24)). For the 5 mm crystal rotations of more than $\pi/2$ are achieved, leading to a turning point within the signal.

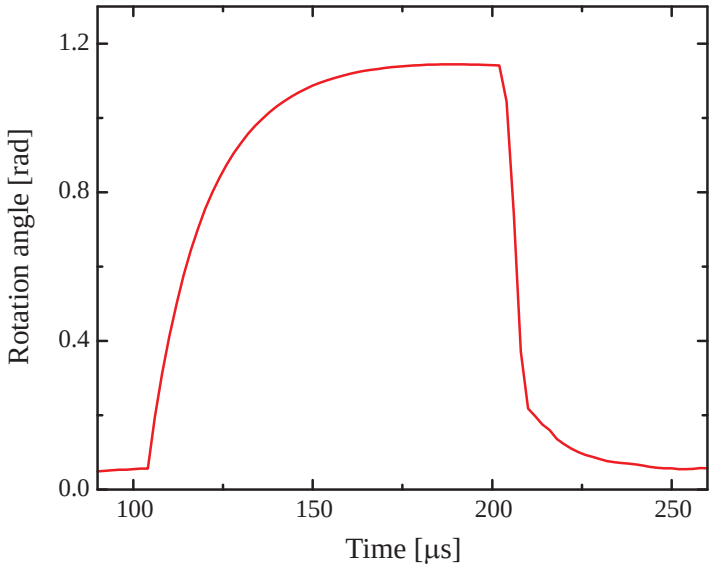


Figure 5.9: The temporal profile of the magnetic field within the coil for a 100 $\mu$s pulse recorded with the 1.40 mm crystal. Within the first 6.6 $\mu$s after the switch off the field drops to 20 % of its original value.

### Results

A magnetic field profile for the 1.4 mm crystal is shown in figure 5.9. The peak magnetic field is calculated by comparing the signal according to equations (2.24) and (5.1) to the integral

$$\frac{1}{d}\int_{-d/2}^{d/2} dz\, B(z) \tag{5.2}$$

where $d$ is the crystal length and $B(z)$ is the magnetic field shown in figure 5.8. During the 100 $\mu$s current pulse the field strength rises slowly until it reaches a 40 $\mu$s plateau. When the current is switched off the field drops linearly to 20 % of its original value within 6.6 $\mu$s and decays then exponentially. The peak magnetic fields obtained from the three different crystal lengths are given in the following table:

| crystal thickness | measured peak $B$-field |
|---|---|
| 1.40 mm | 5.43 T |
| 2.35 mm | 5.05 T |
| 5.00 mm | 5.14 T |

Hence, the average magnetic field is

$$\overline{B} = 5.21 \pm 0.20\,\mathrm{T}. \tag{5.3}$$

Comparison of equation (5.3) with the peak field of $B_{th} = 5.78$ T obtained by finite element analysis (figure 5.8) leads to a discrepancy of 10 %. This can be easily explained since the finite element analysis assumes perfect windings which can never be achieved in the winding process. The wires occupy about 10 % larger volume than ideally anticipated since wires cross on each end of the coil or are not perfectly pulled tight. Hence, the area filled by the windings is larger and the current density lower than modeled.

### 5.1.5 Pulse Generation

We use the same FPGA as described in section 4.1.4 for pulse generation. A graphical user interface in MatLab allows a convenient change of parameters. The communication between computer and FPGA is realized using the serial port.

## 5.2 Results

In this section we present preliminary results we obtained from our first runs with the 64 stage slower.

The slow beam velocity and atom number dependence on the slowing phase is shown in figure 5.10. The phase is kept constant during the slowing process. It is evident that lower phase gives higher detected atom numbers and higher final velocity. The velocity of the slow peak again is calculated by recording a time of flight spectrum with the translation stage retracted, as well as extended. The final velocities are given in table 5.1. The strong noise that can be seen in the spectra with a slow beam is introduced by the firing coils as can be verified by firing the coils without triggering the nozzle. Since the noise is nearly the same on the ground as on the signal line a differential measurement can solve the problem.

Looking at figure 5.10 it is evident that the slow peaks become lower with higher phases. This is partially due to a lower phase space acceptance of the slower at higher phases. Also, a higher phase results in a slower final velocity and the slow beam travels a longer time to the detector. Assuming that the longitudinal velocity

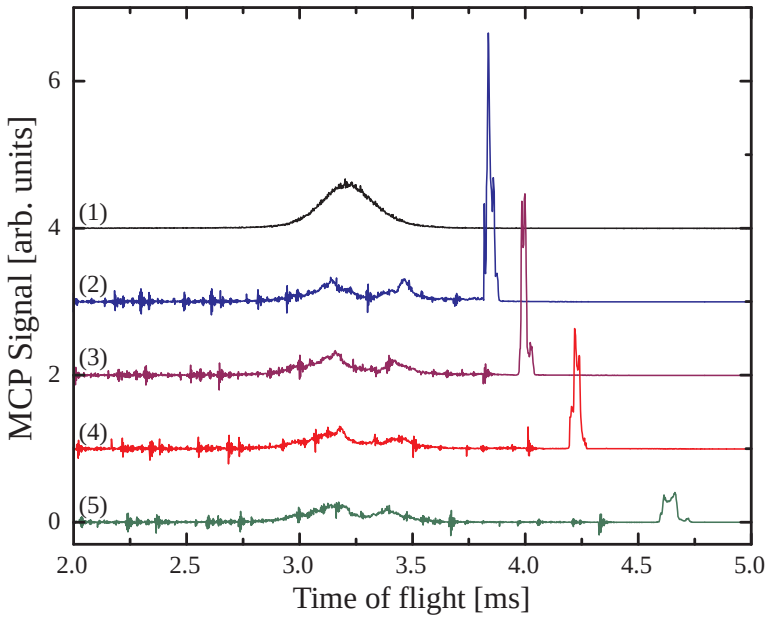


Figure 5.10: Time of flight measurements recorded with the MCP. (1) Reference peak ($v = 447$ m/s), (2) $\phi = 35.8$ ($v = 282$ m/s), (3) $\phi = 38.6$ ($v = 242$ m/s), (4) $\phi = 41.5$ ($v = 203$ m/s), (5) $\phi = 44.3$ ($v = 132$ m/s). Each curve represents an average over 20 shots.. The noise in the curves of the slowed signal is introduced by the firing coils.

| phase angle | final velocity [m/s] | expected velocity [m/s] | rel. atom number |
|---|---|---|---|
| reference | $447 \pm 5$ | – | – |
| 35.8° | $282 \pm 3$ | 278 | 7.6 % |
| 38.6° | $242 \pm 5$ | 243 | 5.3 % |
| 41.5° | $203 \pm 5$ | 199 | 4.2 % |
| 44.3° | $136 \pm 5$ | 132 | 2.1 % |

Table 5.1: Summery of final velocity and atom number estimates for the graphs shown in figure 5.10.

spread is more or less the same for different phases a longer time of flight results in a greater spread of the beam; the signal becomes wider and lower. For the velocities reached with these phases the radial velocity of the slow atoms does not lead to a loss in flux: integrating the area under the peaks in the retracted and extended position yields the same number. That means, that the half angle of the beam is

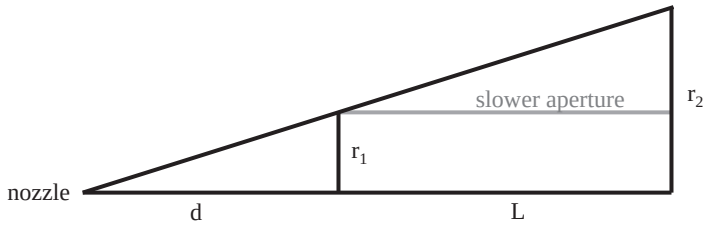


Figure 5.11: Geometry of the slowing apparatus used for number estimates with the distance from the nozzle to the slower $d = 542.6\,\text{mm}$, the radius of the first coil bore $r_1 = 1.5\,\text{mm}$, and the length of the slower $L = 897.7\,\text{mm}$.

smaller than the acceptance angle of the detector $\beta = \arctan(r/l) = 5.7°$ with the detector radius $r = 9\,\text{mm}$ and the distance from the slower exit to the detector $l = 9.08\,\text{cm}$ in the extended position.

In order to get an estimate for our slowing efficiencies, we normalize the area under the slow beams to the area of the reference beam (including all possible spin states) as we expect it to be at the entrance of the slower. Therefore we scale the measured reference beam by taking the slower as a long aperture into account (see figure 5.11): Given the distance from the nozzle to the slower $d = 542.6\,\text{mm}$, the radius of the first coil bore $r_1 = 1.5\,\text{mm}$, and the length of the slower $L = 897.7\,\text{mm}$ we can calculate the radius of the beam at the slower exit if it was not confined through $r_2 = r1 \cdot (d + L)/d = 4\,\text{mm}$ from similar triangles. The squared ratio of $r_2$ to the aperture size at the end of the slower (1.5 mm) is the conversion factor $a = 7.14$. The slowing efficiencies are given in table 5.1. As expected, the phase space acceptance and thus the efficiency is decreased with higher phases.

The finite switching time can lead to a situation where the atom becomes partially re-accelerated after passing the maximum B-field at the center of the coil. This effect is worst for high velocities as there the atom travels the longest distance during the time that is needed to switch off the coil. This consideration leads us to the idea of adjusting the phase: At high velocities we start the switch off at a low phase which is linearly increased with the synchronous atom's velocity.

Allowing a variable phase that is adjusted linearly in velocity over the whole slower like we use in the case of 18 slowing stages (chapter 4.1.2) we find that the slowed atom number decreases compared to a constant phase. We therefore explore this kind of adjustment with a cut off phase, i.e. a maximum phase where we

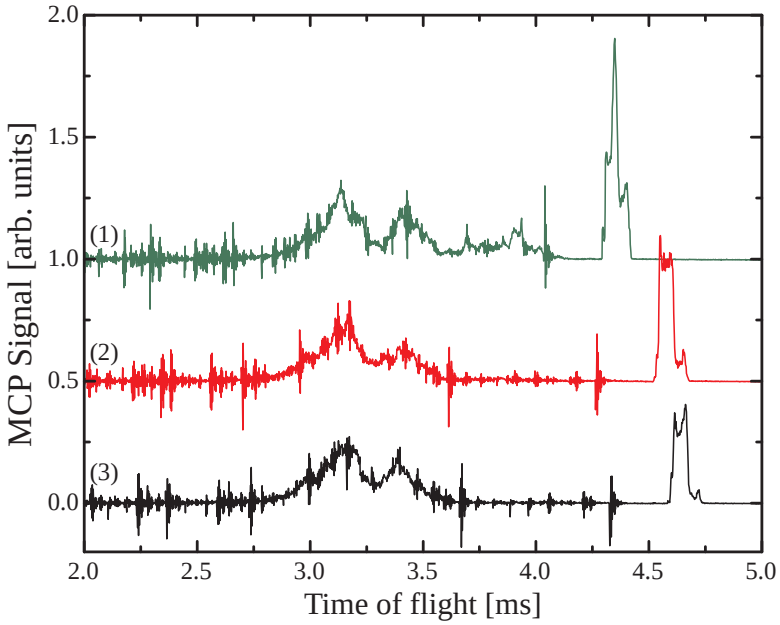


Figure 5.12: Time of flight measurements recorded with the MCP in retracted position. (1) Linear phase adjustment from $\phi_i = 32.9°$ to $\phi_f = 53.6°$ within the first 20 coils ($v_f = 130$ m/s), (2) $\phi_i = 38.6°$, $\phi_f = 46.3°$ within the first 47 coils ($v_f = 136$ m/s), (3) Constant Phase $\phi = 44.3°$ ($v_f = 132$ m/s)

stop the adjustment. To investigate the effect we aim for the same final velocity ($v_f = 136$ m/s). Choosing the start phase and a linear adjustment in velocity determines the final phase.

Some, again preliminary, results are presented in figure 5.12. The final velocities and relative atom numbers are summarized in table 5.2.

| intial phase angle | final phase angle | final velocity [m/s] | rel. atom number |
|---|---|---|---|
| 44.3° | 44.3° | $132 \pm 5$ | 2.1 % |
| 38.6° | 46.3° | $130 \pm 5$ | 3.3 % |
| 32.9° | 53.6° | $136 \pm 5$ | 3.9 % |

Table 5.2: Adjusted phase angles lead to the same final velocity but the slowing efficiency varies by almost a factor 2.

The slowing efficiency can by increased by almost a factor 2 compared to the constant phase case by using an adjusting phase during the slowing process. The

presented data is not complete enough to make out a definite trend. However, the measurements suggest that adjusting phase can lead to greater slowing efficiencies in our slower. Since the success of further experiments will depend strongly on atom numbers a careful characterization of the observed effect will be carried out in the near future.

# Chapter 6

# Conclusions

In this thesis we present a novel and general method to slow supersonic beams of any paramagnetic species using a sequence of pulsed magnetic fields.

Preliminary results which are obtained using a 64 stage slower show deceleration of metastable neon from $447 \pm 3\,\mathrm{m/s}$ to $136 \pm 5\,\mathrm{m/s}$ with an efficiency of up to 3.9 %. We find that the slowing efficiency depends strongly on the switching phase and that an adjustable phase is preferable. It is clear that one has to characterize and understand this effect in detail so that future experiments can profit from high atom numbers and small velocities. Whether it is best to continue the slowing process with a moving trap or whether a simple quadrupole trap is sufficient needs to be investigated.

Once the trapping technique is developed, the window to exciting physics is opened. Never before it has been possible to trap deuterium or tritium. Trapped samples will allow spectroscopic investigations of the isotopic shift between hydrogen and deuterium with higher precision. Having a cold sample of tritium could provide the means to answer one of the most urgent questions in modern physics; the question of the neutrino mass.

# Bibliography


[1] R. Campargue (ed) *Atom and Molecular Beams: The State of the Art 2000* (Springer, Berlin, 2001)

[2] E. Narevicius, A. Libson, M. F. Riedel, C. G. Parthey, I. Chavez, U. Even, and M. G. Raizen, *Coherent Slowing of a Supersonic Beam with an Atomic Paddle*, Phys. Rev. Lett. **98**, 103201 (2007)

[3] M. Gupta and D. Herschbach *Slowing and Speeding Molecular Beams by Means of a Rapidly Rotating Source* J. Phys. Chem. A **105** 1626 (2001)

[4] M. S. Elioff, J. J. Valentini and D. W. Chandler, *Subkelvin Cooling NO Molecules via "Billiard-like" Collisions with Argon*, Science **302** 1940 (2003)

[5] H. L. Bethlem, G. Berden and G. Meijer, *Decelerating Neutral Dipolar Molecules*, Phys. Rev. Lett. **83** 1558 (1999)

[6] R. Fulton, A. I. Bishop and P. F. Barker, *Optical Stark Decelerator for Molecules*, Phys. Rev. Lett. **93** 243004 (2004)

[7] N. Vanhaecke, U. Meier, M. Andrist, B. H. Meier, F. Merkt, *Multistage Zeeman deceleration of hydrogen atoms*, Phys. Rev. A **75** 031402(R) (2007)

[8] S. D. Hogan, D. Sprecher, M. Andrist, N. Vanhaecke and F. Merkt, *Zeeman deceleration of H and D*, Phys. Rev. A **76** 023412 (2007)

[9] G. Scoles, *Atomic and Molecular Beam Methods* (Oxford University Press, New York, 1988)

[10] G. Bronshtein, Master Thesis, *Limit of Relative Velocities for Cluster Onset in Intense Supersonic Beams*, Tel Aviv University (2006)

[11] U. Even, J. Jortner, D. Noy and N. Lavie, *Cooling of large molecules below 1 K and He clusters formation*, J. Chem. Phys. **112** 8068 (2000)

[12] U. Even, M. Hillenkamp and S. Keinan, *Condensation limited cooling in supersonic expansions*, J. Chem. Phys. **118** 8699 (2003)

[13] M. Riedel, Master Thesis, *Elastic Slowing of Supersonic Beams*, The University of Texas at Austin (2006)

[14] Behlke, HTS 31-03-GSM

[15] M. Zinner, P. Spoden, T. Kraemer, G. Birkl, and W. Ertmer, *Precision measurement of the metastable* $^3P_2$ *lifetime of neon*, Phys. Rev. A **67**, 010501(R) (2003)

[16] J. D. Jackson, *Classical Electrodymanics* 3rd ed. (Wiley, New York, 1999)

[17] Carpenter Technology, Permendur 49, ASTM-A-801 Type 1

[18] E. Hecht, *Optics* 4th ed. (Addison-Wesley, 2002)

[19] Northrop Grumman Synoptics

[20] H. L. Bethlem, G. Berden, A. J. A. van Roij, F. M. H. Crompvoets, and G. Meijer, *Trapping Neutral Molecules in a Traveling Potential Well*, Phys. Rev. Lett. **84** 5744 (2000)

[21] S. Humphries, *Principles of Charged Particle Accelerators* (Wiley, New York, 1986).

[22] Matsusada Precision Inc., J4-2N

[23] Stanford Research Systems SR560 Low Noise Preamplifier

[24] Femto, Variable-Gain High-Speed Current Amplifier DHPCA-100

[25] National Instruments, PCI-6120

[26] E. Narevicius, C. G. Parthey, A. Libson, M. F. Riedel, U. Even and M. G. Raizen, *Towards magnetic slowing of atoms and molecules*, New J. Phys. **9** 96 (2007)

[27] B. C. Sawyer, B. L. Lev, E. R. Hudson, B. K. Stuhl, M. Lara, J. L. Bohn, and J. Ye, *Magnetoelectrostatic Trapping of Ground State OH Molecules*, Phys. Rev. Lett. **98** 253002 (2007)

[28] M. Greiner, I. Bloch, T. W. Hnsch and T. Esslinger, *Magnetic transport of trapped cold atoms over a large distance*, Phys. Rev. A **63** 031401 (2001)

[29] E. Narevicius, C. G. Parthey, A. Libson, J. Narevicius, I. Chavez, U. Even and M. G. Raizen, *An atomic coilgun: using pulsed magnetic fields to slow a supersonic beam*, New J. Phys. **9** 358 (2007)

[30] Epoxy Technology, EPO-TEK H77

[31] kepco, RKW 48-2.1K

[32] Powerex, CM400DY-12A

[33] Comsol, FemLab 3.2

[34] C. J. Dedman, K. G. H. Baldwin, and M. Colla, *Fast switching of magnetic fields in a magneto-optic trap*, Rev. Sci. Instrum **72** 4055 (2001)

[35] Xilinx, DS-BD-3SxLC-PQ208 REVISION 2

[36] Varian, Inc., TURBO-V 551 NAVIGATOR, 8 IN. CFF

[37] MKS, 943 Cold Cathode Pressure

[38] Accu-Glass Products, Inc, 600815

[39] Thermionics Vacuum Products, ZC Translator

[40] Powerex, CM200DY-24A

[41] Agilent Technologies, DSO3102A Oscilloscope, 100 MHz

# Vita

| | |
|---|---|
| Place of Birth: | Schlüchtern, Germany |
| Nationality: | German |

**Education**

| | |
|---|---|
| 2006 - 2007 | Graduate Physics Studies at the University of Texas at Austin |
| 2003 - 2006 | Physics Studies at the Julius-Maximilians-University of Würzburg |
| 2002 - 2003 | Social Service at Hamm Kliniken, Bad Soden-Salmünster |
| 1993 - 2002 | Ulrich-von-Hutten Gymnasium, Schlüchtern |

**Fellowships and Prizes**

| | |
|---|---|
| 2006 | DAAD Fellowship |
| 2006 | C. Paul Boner Graduate Fellowship in Physics |
| 2001 | Prize of the DPG (German Physical Society) for outstanding performance in the subject Physics |

**Publications**

E. Narevicius, A. Libson, M. F. Riedel, C. G. Parthey, I. Chavez, U. Even, and M. G. Raizen, *Coherent Slowing of a Supersonic Beam with an Atomic Paddle*, Phys. Rev. Lett. **98**, 103201 (2007)

E. Narevicius, C. G. Parthey, A. Libson, M. F. Riedel, U. Even and M. G. Raizen, *Towards magnetic slowing of atoms and molecules*, New J. Phys. **9** 96 (2007)

E. Narevicius, C. G. Parthey, A. Libson, J. Narevicius, I. Chavez, U. Even and M. G. Raizen, *An atomic coilgun: using pulsed magnetic fields to slow a supersonic beam*, New J. Phys. **9** 358 (2007)

Permanent Address: Christian Parthey
Weilersweg 31
63628 Bad Soden-Salmünster
Germany

This thesis was typeset with LaTeX $2_\varepsilon$[1] by the author.

[1] LaTeX $2_\varepsilon$ is an extension of LaTeX. LaTeX is a collection of macros for TeX. TeX is a trademark of the American Mathematical Society. The macros used in formatting this thesis were written by Dinesh Das, Department of Computer Sciences, The University of Texas at Austin, and extended by Bert Kay, James A. Bednar, and Ayman El-Khashab.